

1 **Dynamic fault interaction during a fluid-injection induced earthquake: The**
2 **2017 Mw 5.5 Pohang event**

- 3 • **Kadek Hendrawan Palgunadi¹** : kadek.palgunadi@kaust.edu.sa
4 • **Alice-Agnes Gabriel²** : gabriel@geophysik.uni-muenchen.de
5 • **Thomas Ulrich²** : ulrich@geophysik.uni-muenchen.de
6 • **José Ángel López-Comino³ⁱ** : lopezcomino@uni-potsdam.de
7 • **Paul Martin Mai¹** : martin.mai@kaust.edu.sa

- 8
9 1. Physical Science and Engineering, King Abdullah University of Science and Technology, Thuwal, Saudi Arabia
10 2. Department of Earth and Environmental Sciences, Geophysics, Ludwig-Maximilians-Universität München,
11 Theresienstr. 41, 80333 Munich, Germany
12 3. Institute of Geosciences University of Potsdam, Potsdam-Golm, Germany.
13

ⁱalso at Instituto Andaluz de Geofísica, Universidad de Granada, Spain; Departamento de Física Teórica y del Cosmos, Universidad de Granada, Spain; Physical Science and Engineering, King Abdullah University of Science and Technology, Thuwal, Saudi Arabia

14 **Abstract:**

15 The November 15th, 2017 Mw 5.5 Pohang earthquake (South Korea) has been linked to hydraulic
16 stimulation and fluid injections, making this the largest induced seismic event associated with an
17 Enhanced Geothermal System (EGS). To understand its source dynamics and fault interactions,
18 we conduct the first 3D high-resolution spontaneous dynamic rupture simulations of an induced
19 earthquake. We account for topography, off-fault plastic deformation under depth-dependent bulk
20 cohesion, rapid velocity weakening friction and 1D subsurface structure. A guided fault
21 reconstruction approach that clusters spatio-temporal aftershock locations (including their
22 uncertainties) is used to identify a main and a secondary fault plane which intersect under a shallow
23 angle of 15°. Based on simple Mohr-Coulomb failure analysis and 180 dynamic rupture
24 experiments in which we vary local stress loading conditions, fluid pressure, and relative fault
25 strength, we identify preferred two fault plane scenarios that well reproduce observations. We find
26 that the regional far-field tectonic stress regime promotes pure strike-slip faulting, while local
27 stress conditions constrained by borehole logging generate the observed thrust faulting component.
28 Our preferred model is characterized by overpressurized pore fluids, non-optimally oriented but
29 dynamically weak faults and a close to critical local stress state. In our model, earthquake rupture
30 “jumps” to the secondary fault by dynamic triggering, generating a measurable non-double couple
31 component. Our simulations suggest that complex dynamic fault interaction may occur during
32 fluid-injection induced earthquakes and that local stress perturbations dominate over the regional
33 stress conditions. These findings, therefore, have important implications for seismic hazard in
34 active geo-reservoir.

35

36

37 **Introduction**

38 The Korean Peninsula is known to have a rather low-level of seismicity (compared to
39 neighboring countries like China and Japan) because it lies on the continental margin of the east
40 Eurasian plate. However, on November 15th, 2017 (05:29:31 UTC), a magnitude Mw 5.5
41 earthquake occurred (hereinafter the Pohang earthquake), the second-largest recorded earthquake
42 in South Korea following the 2016 M_L 5.8 Gyeongju earthquake. The Pohang earthquake caused
43 one fatality, injured 82 people, and generated more than \$300 millions in total economic loss
44 (Ellsworth et al., 2019; Lee et al., 2019). The hypocenter was located approximately 10 km
45 northeast of Pohang city, close to the Pohang Enhanced Geothermal System (EGS) site (36.106°N,
46 129.373°E and depth ~4.27 km, Korean Government Commission, 2019). Its proximity to the EGS
47 site and hypocentral depth similar to the open hole sections of the fluid-injection wells (Figure 1)
48 quickly raised questions if this earthquake is associated with EGS activities (Grigoli et al., 2018;
49 Kim et al., 2018).

50 The Pohang EGS project was designed to create an enhanced geothermal reservoir within
51 a low permeability crystalline basement. The basement is overlain by cretaceous volcanic and
52 sedimentary rocks, tertiary volcanic and sedimentary rocks, and quaternary sediments (Korean
53 Government Commission, 2019; Ellsworth et al., 2019). During a period of four years (2012 to
54 2016), two geothermal wells (maximum depth ~4.3 km) were drilled for hydraulic stimulations.
55 At the surface, both wells are separated by only 6 m distance, increasing to a separation of 599 m
56 at a depth of ~4.3 km. For well PX-1, the drilling was stuck at a depth of 2419 m, and hence side-
57 tracked into west-northwest direction. Well PX-2 experienced large mud loss in the depth interval
58 3830 - 3840 m, while cuttings contain significant fractions of friable round-shaped mud balls
59 typical for fault gouge (Korean Government Commission, 2019; Ellsworth et al., 2019). In these

60 geothermal wells, five hydraulic stimulations were conducted between 29 January 2016 and 18
61 September 2018. During this period, each hydraulic stimulation phase was associated with
62 seismicity. The magnitudes during and after stimulations reached up to $M_L \approx 3$, while events were
63 distributed within a restricted area close to the wells (Woo et al., 2019). The depth of the seismicity
64 before the Pohang earthquake spans the depth range 3.8 to 4.4 km, comparable with the open-hole
65 section of the well at ~ 4.3 km depth (Ellsworth et al., 2019).

66 Recent studies confirm that the Pohang earthquake was induced by hydraulic stimulation
67 and extensive fluid injection at this EGS site (Korean Government Commission, 2019; Ellsworth
68 et al., 2019; Woo et al., 2019; Kim et al., 2020). These activities are considered to have activated
69 the previously unmapped fault which was found to intersect well PX-2 at a depth of ~ 3.8 km.
70 Chang et al. (2020) point out that increased pore-pressure stressing due to multiple injection wells
71 at the Pohang EGS site may have contributed to the mainshock generation. However, it has been
72 argued that the size of fluid-injection induced earthquakes can be controlled by managing pressure,
73 location, and rate of fluid injection (Hofmann et al., 2019). Data-driven empirical and numerical
74 studies have shown that the induced earthquakes are confined by a function of injected volume
75 (McGarr, 2014; Galis et al., 2017).

76 Grigoli et al. (2018) find a complex-source mechanism for the Pohang earthquake with a
77 significant non-double couple (non-DC) component. They hypothesized that this earthquake
78 involved failure on two different faults with slightly different focal mechanisms. In fact, in EGS
79 reservoirs with extensive fluid injection and hydraulic stimulation, earthquakes with pronounced
80 non-DC components may occur (Julian et al., 1998). Moreover, fluid injections may induce local
81 deviation of the stress state from the regional stress regime (Schoenball et al., 2014; Martínez-
82 Garzón et al., 2013; Martínez-Garzón et al., 2014). Therefore, we examine how regional and local

83 stress conditions acting on different fault models (single plane and two planes) determine the
84 dynamic rupture process that leads to a source mechanism with non-DC components.

85 Dynamic rupture modeling aims to reproduce the physical processes that govern how
86 earthquakes start, propagate, and stop for given stress and frictional conditions acting on fault
87 surfaces. The earthquake dynamics are then a result of the model's initial conditions, such as
88 geometry and frictional strength of the fault(s), the tectonic stress state, the regional lithological
89 structure, and a frictional constitutive equation. Jin and Zoback (2018) model coseismic fully
90 dynamic spontaneous fault rupture resulting from preseismic quasi-static loading exerted by fluid
91 perturbations in a faulted porous medium in 2D. Duan (2016) model 2D dynamic rupture
92 accounting for fluid effects of a propagating hydraulic fracture. Cappa and Ruitquist (2012) and
93 Buijze et al. (2017) constrain the onset of 2D dynamic rupture experiments by the stress state
94 resulting from solving a coupled quasi-static poroelastic equation. Further 2D studies that model
95 induced (not fully dynamic) earthquake rupture linked to separately treated fluid diffusion
96 including Galis et al. (2017); Kroll et al., (2017); Dieterich et al. (2015); Garagash and
97 Germanovich (2012); Richards-Dinger and Dieterich (2012); Viesca and Rice (2012). Using
98 modern numerical methods and advanced hardware, a high degree of realism can be reached to
99 explicitly model in 3D the highly non-linear dynamic rupture process (e.g., Heinecke et al., 2014;
100 Roten et al., 2014; Uphoff et al., 2017; Wollherr et al., 2019; Ulrich et al., 2019a, 2019b). The
101 modeling results include spatial and temporal evolution of earthquake rupture, surface
102 displacements, and ground shaking caused by the radiated seismic waves.

103 In this study, we investigate the dynamic rupture process under variable stress and fault-
104 geometry assumptions for the Pohang earthquake, using the high-performance-computing (HPC)
105 enabled software package SeisSol (see **Data and Resources**). Two alternative fault geometries are

106 considered, a one fault plane model (Model 1F) and a two fault planes model (Model 2F). In our
107 simulations, we consider a 1D velocity structure (Woo et al., 2019), off-fault plasticity (Wollherr
108 et al., 2018), depth-dependent bulk cohesion, a rapid velocity weakening friction law, borehole
109 estimates of stress, complex fault geometry, and high-resolution topography.

110 In the following, we first describe (Section 2) a new observationally guided fault
111 reconstruction approach based on spatio-temporal clusters of microearthquakes and their spatial
112 uncertainty. In Section 3, we analyse initial fault strength and loading stresses using static and
113 dynamic rupture modeling. We then compare the dynamics and kinematics of two preferred
114 models, Model 1F and 2F. The validation of Model 2F with regional waveforms, as well as
115 comparison of surface deformation between Model 1F and Model 2F are also presented in Section
116 3. Finally, we discuss the importance of considering local stresses loading, apparently weak and
117 critically stressed faults, overpressurized fluids, and dynamic multiple fault interaction in EGS.

118

119 **Modeling Setup**

120 In the following, we describe our approach to produce a physically viable model
121 constrained by observational data. Dynamic rupture propagation is governed by fault strength,
122 fault geometry, subsurface material properties, topography, loading (“initial”) stresses, nucleation
123 procedure, and empirical friction laws (Dunham et al., 2011a; Harris et al., 2011; Harris et al.,
124 2018). Numerical experiments that vary the aforementioned parameters provide insights into
125 fundamental earthquake physics as well as serve to identify preferred, self-consistent scenarios
126 that explain the mechanical processes of the earthquake as well as observational data.

127

128 **Fault reconstruction**

129 The detailed fault geometry has a strong effect on the dynamic rupture process. Changes
130 in strike, dip, and deviations from fault planarity can impact the rupture propagation and the
131 corresponding physical processes. The Pohang earthquake occurred on one or several blind and
132 unmapped fault(s). Because the unwrapped InSAR surface-displacement data show unclear fringes
133 due to the small deformation around the epicenter (Choi et al., 2019; Song and Lee, 2019), we use
134 the high-resolution earthquake catalog from Kim et al. (2018) to constrain the fault geometry based
135 on a space-time (including their uncertainties in space) clustering approach. The earthquake
136 catalog spans from 9 hours before to 3 hours after the mainshock and contains 217 events.

137

138 **Spatio-temporal clustering**

139 Clustering techniques allow deciphering complex fault structures by associating seismic
140 events to groups (clusters), also discriminating events that are associated with the mainshock from
141 uncorrelated earthquakes. We examine the seismic sequence to separate seismic clusters and
142 background events using nearest-neighbor distances following Zaliapin and Ben-Zion (2013). The
143 dependence of an event i to a parent event j is determined from the nearest-neighbor distance η_{ij} :

144

$$145 \quad \eta_{ij} = dt_{ij} \times dr_{ij}^d, d_{ij} > 0; \eta_{ij} = \infty, dt_{ij} < 0 \quad (1)$$

146

147 where $dt_{ij} = t_j - t_i$ is the time between event i and j , $dr_{ij} = (r_j - r_i)$ is the interevent distance
148 between events; r_i = coordinate of event i and r_j = coordinate of event j , and d is the fractal
149 dimension of the earthquake hypocenter distribution (Hirata, 1989). We find that the inferred
150 clusters are not very sensitive to the parameter d ; hence we set $d = 1.6$ following previous studies
151 (Zaliapin and Ben-Zion, 2013; Zhang and Shearer, 2016; Cheng and Chen, 2018). Based on this

152 analysis, we find that all earthquakes of the catalog are part of the cluster and can be used for fault-
153 plane fitting (see Figure 2a). This cluster is characterized by interevent distances less than 1 km.

154

155 **Fault plane fitting**

156 We adopt the anisotropic clustering location uncertainty distribution (ACLUD) method, a
157 fault-network reconstruction approach introduced by Wang et al. (2013), which accounts for
158 uncertainties in earthquake locations. This method is extended by considering regional tectonic
159 constraints, focal mechanisms, and surface geological manifestation as prior information, leading
160 to the following improvements in the original ACLUD algorithm:

- 161 1) Initialize N_0 number of faults following the predefined orientation of the S_{Hmax} extracted
162 from the world stress map with random position and size.
- 163 2) For each cluster, if more than four similar focal mechanisms (strike, dip, rake) are available,
164 we use this information to separate events that have distinct focal mechanisms into other
165 clusters.
- 166 3) If surface geological manifestation (fault traces) exists (not the case for this study), the
167 strike and dip of the generated fault segment(s) should follow the closest interpreted fault
168 trace orientation.

169 We refer to this modified ACLUD method as guided-ACLUD (g-ACLUD).

170 All explored solutions are subject to a statistical validation process that examines the
171 likelihood of each proposed fault-network, given all available focal mechanisms. Statistical
172 validation uses the Bayesian Information Criterion (BIC). Initially, the method uses a random
173 number of fault planes. A single fault plane may be split if the BIC remains high. On the other
174 hand, two close-enough fault planes with similar orientation (strike and dip) may be merged into

175 a single fault plane. The process is repeated until the BIC reaches a pre-defined minimum or if the
176 process exceeds the maximum specified number of iterations (Wang et al., 2013).

177 The ACLUD algorithm by Wang et al. (2013) uses event locations and the associated
178 uncertainties given by the earthquake catalog. We incorporate additional information to increase
179 the robustness of the results and to decrease the explored parameter space. As *a priori* information,
180 we use the orientation of the maximum compressive regional stress given by the world stress map
181 (Heidbach et al. 2018) and available focal mechanisms in the area which are associated with the
182 earthquake catalog. Therefore, we use a maximum horizontal stress orientation of 74° with an
183 uncertainty of 25° and consider the focal mechanism inferred by Grigoli et al. (2018). Since
184 location errors are not specified in this earthquake catalog, we assume normally distributed
185 uncertainty for all events (standard deviation of 100 m). Note that Kim et al. (2018) obtained a
186 median error of 42, 31, and 36 m in the EW, NS, and vertical directions, respectively, but no
187 uncertainties for individual events.

188 Figure 2b, 2c, 2d show the g-ACLU selected solution, characterized by the smallest BIC,
189 which features two intersecting planar fault planes. The main plane strikes at 214° and dips at 65° ,
190 while the secondary fault plane strikes at 199° and dips 60° , respectively. The two fault planes are
191 separated by a narrow angle of 15° . The secondary fault aligns with the subsidiary fault plane
192 identified by Kim et al. (2018). The dimensions of the main and secondary fault planes are 4.3 km
193 x 2.8 km and 3.0 km x 2.2 km, respectively. As the goal of this study is to compare the rupture
194 process for two different fault configurations, we define a one fault plane geometry (Model 1F)
195 and a two fault planes geometry (Model 2F; derived fault reconstruction analysis). The single-fault
196 model has a fault plane striking 214° and dipping 43° , as suggested by Korean Government
197 Commission (2019), Ellsworth et al. (2019), and Woo et al. (2019).

198

199 **Material properties**

200 We assume an elasto-plastic, isotropic medium based on the 1D velocity profile (Figure
201 S1a; Woo et al. (2019)). The velocity profile honors geological structures observed from drilling
202 cores and seismological observations from both active and passive sources, for instance, vertical
203 seismic profiling (VSP) and well logging (Korean Government Commission, 2019; Woo et al.,
204 2019). The density distribution (Figure S1a) is adopted from the report by Korean Government
205 Commission (2019).

206 We use a computationally efficient implementation of a Drucker-Prager off-fault
207 viscoplastic rheology (Wollherr et al., 2018). The off-fault failure criterion is based on the internal
208 friction coefficient (bulk friction) and bulk cohesion. We assume a constant internal friction
209 coefficient equal to the prescribed on-fault friction coefficient ($\mu_{bulk-friction} = 0.6$) for the entire
210 model domain. However, bulk cohesion is set to be depth-dependent, accounting for geologic
211 strata in the Pohang EGS site and the hardening of rocks with depth. Therefore, bulk cohesion
212 ranges from $c = 4$ MPa near the surface to $c = 50$ MPa at a depth of 6 km. A lower bulk cohesion
213 (12.5% of the surroundings) is applied in a $1.5 \times 0.3 \times 4$ km³ volume around the fault intersection
214 for the case of two fault planes to mimic pre-existing damage which enhances off-fault yielding
215 and to prevent unrealistic high on-fault stresses at the fault intersection. We assume initially
216 equivalent stresses acting on and off the fault. Finally, we set a constant, mesh-independent
217 relaxation time following the analysis by Wollherr et al., (2018) and chose $T_V = 0.05$ s, consistently
218 with choices made in previous studies (e.g. Ulrich et al., 2019a, 2019b).

219

220 **Fault strength and loading stresses**

221 To constrain the most viable principal stress component azimuth and the overall stress
222 regime, we extract information (e.g., S_{Hmax} orientation and fault strength) from laboratory and
223 field observation to then perform numerical experiments. We adopt a friction law with rapid
224 velocity weakening (adapted from Dunham et al., 2011a; see Appendix, **Friction parameters**)
225 which reproduces the rapid friction decrease observed in laboratory experiments at co-seismic slip
226 rates (Di Toro et al., 2011).

227 We parametrize fault friction aiming for realistic levels of static and dynamic frictional
228 resistance and stress drop. All frictional properties are detailed in Appendix (**Friction**
229 **parameters**). We apply velocity weakening ($b - a = 0.004$) across the fault (see Figure S1b) and
230 velocity strengthening ($b - a = -0.004$) to the uppermost part of the fault, which allows for a
231 smoother termination of the rupture there. The state evolution distance (L), initial slip rate (V_{ini}),
232 reference slip velocity (V_0), steady-state friction coefficient (f_0), and weakened friction coefficient
233 (f_w) are constant and depth-independent.

234 We follow the systematic approach of Ulrich et al. (2019a) to examine initial fault stress
235 and relative apparent fault strength combining data from observations, (e.g., seismo-tectonic
236 observations and fault fluid pressurization) and the Mohr-Coulomb theory of failure. This
237 workflow reduces the non-uniqueness in dynamic rupture modeling parameterization by assessing
238 that the stress state is compatible with the fault geometry and the fault-slip orientation (rake angle)
239 inferred from finite source or moment tensor inversion. Assuming an Andersonian stress regime
240 (one principal stress axis is vertical), only four parameters are sufficient to fully describe the stress
241 state and strength of the fault system: the azimuth of maximum compressive stress (S_{Hmax}), the
242 initial relative fault prestress ratio (R_0), the stress shape ratio (ν), and the fluid pressure ratio (γ),
243 all detailed hereafter.

244 The Pohang EGS site is considered to be located within a strike-slip stress regime (Soh et
245 al., 2018, and references therein). This translates into the maximum principal stress being
246 horizontal ($s_1 = S_{Hmax}$, with principal stress components $s_1 > s_2 > s_3 > 0$) under Andersonian
247 stress. Previous studies examined the azimuth of maximum horizontal stress using different
248 methods, such as borehole and seismological techniques, e.g., stress inversion of focal mechanisms
249 (Kim et al., 2017; Lee et al., 2017; Lee, Hong, and Chang, 2017; Soh et al., 2018; Korean
250 Government Commission, 2019; Ellsworth et al., 2019). Soh et al. (2018) inferred S_{Hmax} from
251 focal mechanisms of earthquakes that occurred between 1997 and 2016 and determined a regional
252 $S_{Hmax} = 74^\circ$. However, the earthquakes closest (~40 km) to the Pohang EGS site used in their
253 analysis are the 2016 Gyeongju event and its aftershocks. Based on borehole data, Kim et al. (2017)
254 and Lee, Shinn, et al. (2017) determined that S_{Hmax} at shallow depths (700 m to 1000 m) within a
255 10 km radius from the Pohang EGS is about 130° . In contrast, Ellsworth et al. (2019) and Korean
256 Government Commission (2019) inferred a critically stressed thrust faulting regime. This stress
257 state implies that the vertical stress is the least principal stress under Andersonian stress ($s_v = s_3$).
258 They inferred an S_{Hmax} orientation of $77 \pm 23^\circ$ based on dipole sonic logging data. This
259 orientation is similar to the value of 74° given in the world stress map (Heidbach et al., 2018).

260 Using numerical simulations, we then assess how these loading-stress regimes for the
261 inferred fault geometry determine nucleation and rupture of the Pohang earthquake. The stress
262 shape ratio ν enables a contrast of different stress styles by balancing the principal stress
263 amplitudes. It is defined as:

264

$$265 \quad \nu = \frac{(s_2 - s_3)}{(s_1 - s_3)} \quad (2)$$

266

267 For strike-slip regimes (s_2 vertical), $\nu < 0.5$ characterizes transpression, $\nu \approx 0.5$ corresponds to
268 pure strike-slip regime, and $\nu > 0.5$ characterizes transtension (Ulrich et al., 2019a). Soh et al.
269 (2018) ($\nu = 0.12$), Ellsworth et al., (2019) and Korean Government Commission (2019) ($\nu = 0.1$)
270 suggests a stress regime acknowledging transpression around the Pohang EGS site (note that they
271 use different definition of ν).

272 The initial relative prestress ratio (R_0) describes the closeness to failure on a virtual,
273 optimally oriented fault. $R_0 = 1$ indicates a critical stress level on all optimally oriented faults. We
274 can characterize fault strength spatially by calculating the relative prestress ratio (R) on every point
275 of the fault. R denotes the ratio of potential stress drop $\Delta\tau$ with respect to breakdown strength drop
276 $\Delta\tau_b$ for given frictional cohesion (c), static (μ_s) and dynamic (μ_d) friction coefficient (e.g., Aochi
277 and Madariaga, 2003) expressed as:

278

$$279 \quad R = \frac{\Delta\tau}{\Delta\tau_b} = \frac{\tau_0 - \mu_d \sigma_n}{c + (\mu_s - \mu_d) \times \sigma_n} \quad (3)$$

280

281 where τ_0 and σ_n are initial shear and normal traction on the fault plane, respectively. However, in
282 this study, we neglect the contribution of frictional cohesion ($c = 0$), which is mostly important to
283 incorporate close to the Earth's surface. We assume $\mu_s = f_0 = 0.6$ and $\mu_d = f_w = 0.1$. The
284 relative prestress ratio can be related to the relative fault strength parameter (S) defined as $S =$
285 $1/R - 1$. On-fault values of R change at every point as we vary R_0 , taking on values $R \leq R_0$
286 depending on the orientation of each fault point with respect to the optimal orientation.

287 The vertical principal stress is assumed to vary linearly with depth, consistent with the
288 geological strata (depth-dependent density (ρ) in Figure S1a). We assume the intermediate

289 principal stress component, s_2 , to be vertical. The confining pressure of the overlying rock is
290 reduced by the pore pressure (P_f). We assume P_f proportional to lithostatic stress as $P_f = \gamma \rho g z$,
291 where g is the gravitational acceleration (9.8 m/s^2), and z denotes depth (in meters) and γ is the
292 fluid pressure ratio. A fluid pressure ratio of 0.37 indicates hydrostatic pore pressure, while $\gamma >$
293 0.37 implies an overpressurized stress state.

294 We perform a range of static and dynamic numerical experiments described below to test
295 the sensitivity of the resulting dynamic rupture models to the chosen stress parameterization in
296 terms of S_{Hmax} , R_0 and γ . We keep the 4th parameter, the stress shape ratio, fixed at $\nu = 0.12$
297 (Soh et al., 2018). We do not adjust the stress states for the stress excess during nucleation (see
298 Appendix, **Nucleation procedure**). The overstressed nucleation and its parameters are constant
299 for all 180 numerical experiments.

300

301 **Results**

302 We use the open-source software SeisSol (details in Appendix, **numerical method**) to
303 solve the elastodynamic equations of motion for fault rupture under stress and friction acting on
304 the fault surface, coupled to seismic wave propagation in complex media. We set the on-fault mesh
305 size using estimates of cohesive zone width (details in Appendix, **mesh generation**). We
306 incorporate high-resolution topography into our modeling. Figure 3 shows the computational mesh
307 overlain by a snapshot of absolute velocity at $t = 5 \text{ s}$.

308 Next, we present 3D dynamic rupture simulations for scenarios that consider one and two
309 intersecting fault planes, incorporating depth-dependent regional loading stresses, off-fault plastic
310 yielding, and high-resolution surface topography. In the preferred model (Model 2F), the
311 secondary fault plane is dynamically triggered and can explain the observed non-double couple

312 component of the moment tensor solution. Our model is compatible with regional waveforms and
313 surface deformation derived from published InSAR analysis.

314

315 **Static and dynamic analysis of initial fault strength and stresses**

316 We first constrain the regional stress from purely static analysis. Figure S2 shows a few
317 cases (out of many permutations (see also Table S1)) we analyzed. The six examples shown use
318 parameters $\gamma = 0.5$ and $R_0 = 0.7$, and variable S_{Hmax} in the range $52^\circ - 140^\circ$. According to the
319 static analysis, $S_{Hmax} < 87^\circ$ is insufficient to generate a rake angle of shear traction compatible
320 with the thrust-faulting component inferred by the focal mechanism and moment tensor solution.
321 At $S_{Hmax} \geq 87^\circ$, a thrust-faulting component starts to emerge. Interestingly, only the secondary
322 fault plane features a rake angle larger than 40° for $S_{Hmax} = 77^\circ - 140^\circ$. A rake angle of $\sim 80^\circ$,
323 obtained with $S_{Hmax} = 120^\circ$, can potentially produce the thrust-faulting component inferred by
324 moment tensor solution. For this parametrization, the secondary fault plane reaches a higher rake
325 angle of approximately 110° .

326 We restrict the parameter space for R_0 and γ based on our static analysis. We then
327 systematically explore all permutations of the three different parameters within the selected range
328 using dynamic rupture simulations. We vary R_0 in the range $0.7 - 0.9$, γ within $0.37 - 0.9$ and
329 S_{Hmax} within $67 - 120^\circ$. Figure 4 summarizes the outcome of 180 numerical dynamic rupture
330 experiments. We find that under hydrostatic pressure ($\gamma = 0.37$), $S_{Hmax} = 120^\circ$ generates self-
331 sustained ruptures over any other S_{Hmax} orientation.

332 The thrust-faulting component generated with $S_{Hmax} = 67^\circ - 87^\circ$ is insufficient to
333 explain the seismological observation using dynamic rupture modeling. Such S_{Hmax} leads to pure
334 strike-slip faulting as the only mechanical viable solution. Both dynamic and static analyses

335 suggest that $S_{Hmax} = 120^\circ$ is necessary to generate a thrust-faulting component close to the
336 observations. Our analyses allow determining a preferred parameterization, compatible with
337 inferred ground deformation, observed regional waveforms, and the inferred focal mechanism:
338 $R_0 = 0.8$ and $\gamma = 0.5$.

339

340 **Rupture dynamics of the preferred scenario Model 1F and Model 2F**

341 Figure 5a and Video S1 (in supplementary material) provide an overview of the simulated
342 earthquake rupture of the preferred two fault model Model 2F: rupture propagates spontaneously
343 across the main fault plane and dynamically triggers the secondary fault plane (rupture jumping).

344 The rupture nucleates smoothly due to the prescribed time-dependent overstress (see
345 Appendix, **Nucleation procedure**) centered at the hypocenter location; it then spontaneously
346 propagates bilaterally across the main fault plane. At a rupture time of 0.65 s, two successive slip-
347 rate fronts emerge, with lower peak slip rates than the main rupture front (Figure 5a, left). This
348 rupture complexity is associated with the simultaneous rupture on both fault planes, leading to
349 multiple reflected and trapped waves in-between the two fault planes, reactivating the main fault
350 around the intersection. Rupture complexity decreases as rupture on the secondary fault plane
351 terminates. After rupture time $t = 0.75$ s, we observe solely pulse-like rupture propagation across
352 the main fault.

353 The secondary fault plane is dynamically triggered at 0.4 s and its rupture terminates at 0.8
354 s simulation time, while the main-fault is fully ruptured in about 1.1 s. The secondary fault plane
355 is only partially ruptured because the northern part of the main fault does not slip. High slip-rates
356 (~ 10 m/s) and multiple rupture fronts occur near the fault intersection at the secondary fault.
357 Rupture heals close to the fault intersection region around $t = 0.65$ s.

358 After $t = 0.75$ s rupture on the main fault dynamically clamps (e.g., Kyriakopoulos et al.,
359 2019) and thus does not facilitate direct branching to the northern unbroken part of the secondary
360 fault plane. We observe asymmetric peak slip-rate distribution (see Figure S3), with higher values
361 on the single fault plane part of the network (Figure 5a, right) and lower peak slip rates where
362 ruptures across directly adjacent fault planes interact, which is also associated with high off-fault
363 plastic yielding (see section **Off-fault deformation** below). The entire rupture is completed after
364 ~ 1.5 s simulation time, breaking 4 km of fault length and generating a moment magnitude of M_w
365 5.59 (dominated by slip on the main fault plane). We find that rupture stops smoothly and
366 spontaneously on the secondary fault plane and north-eastern part of the main fault plane, while
367 being stopped abruptly by the southwestern fault end of the main fault plane.

368 In contrast to the Model 2F, the one fault plane preferred Model 1F produces symmetric
369 bilateral slip-rate and slip distributions.

370

371 **Rupture kinematics of the preferred Model 1F and Model 2F scenarios**

372 Due to the size of the event and limited available data, the kinematics of the Pohang
373 earthquake are challenging to characterize and explain. We here describe the model kinematics of
374 the preferred Model 1F and Model 2F earthquake scenarios. and compare both with two
375 observational studies (Song and Lee, 2019; Grigoli et al., 2018).

376 Song and Lee (2019) estimated the static slip distribution by InSAR (both descending and
377 ascending-descending orbit) for a single fault plane with patch size 0.5 by 0.5 km. Higher slip
378 predominantly occurs northeast of the hypocenter, with an average slip of 0.15 m (Song and Lee,
379 2019). Grigoli et al. (2018) applied an Empirical Green's Function (EGF) technique to study
380 rupture duration and directivity, suggesting an apparent rupture duration of ~ 1 s and ~ 3 s for

381 stations observed in the SE and NW direction, respectively. Their focal mechanism shows an
382 average rake of $\sim 135^\circ$.

383 Both preferred scenarios vary slightly in moment magnitude, M_W 5.63 and M_W 5.59 for
384 Model 1F and Model 2F, reflecting different fault geometries while otherwise using the same
385 dynamic rupture model parametrization. We point out that most slip of Model 2F occurs on the
386 main fault - its magnitude is reduced to M_W 5.51 when removing the subsidiary plane.

387 The resulting synthetic source time functions of Model 1F and Model 2F are presented in
388 Figure 6a and 6b, respectively. The boxcar shaped moment rate function of Model 1F results from
389 its comparably simple rupture dynamics across one planar fault. Model 2F features a more
390 complicated moment rate function featuring two peaks of which the first one is reached at $t = 0.5$
391 s simulation time during simultaneous rupture of both fault planes. The rupture duration of both
392 scenarios is less than 1.5 s. The moment tensor representations of Model 1F and Model 2F are
393 presented in Figure 6c and 6d, respectively. Both scenarios show oblique faulting mechanisms.
394 Model 1F clearly produces a double-couple moment tensor solution (Figure 6c), whereas the
395 Model 2F yields a non-double couple solution due to complex source mechanism (Figure 6d), in
396 agreement with Grigoli et al. (2018). Nevertheless, our simulation produces a smaller amount of
397 CLVD (compensated linear vector dipole) compared to Grigoli et al. (2018). In fact, the equivalent
398 moment tensor solution of Model 2F can be decomposed, following the methodology of Vavryčuk
399 (2015), into 82.95% DC, -5.05% CLVD, and -12% isotropic (ISO) components. In contrast,
400 Grigoli et al. (2018) find -37% CLVD. In our simulations, Model 2F's rupture is characterized by
401 an average rupture speed of $v_r \approx 2,250$ m/s, well below the average Rayleigh wave speed at the
402 depth of the faults ($v_r \sim 0.75V_S$). The spatial variation of v_r is mainly related to the complexity of
403 rupture around the intersection for both, the main and secondary fault plane. We observe higher

404 average rupture speed $v_r \approx 2,780 \text{ m/s}$ ($v_r \sim 0.8V_S$) on the secondary fault plane (see rupture
405 contours every 0.2 s in Figures 5b, 5c). We note the localized occurrence of supershear rupture
406 speeds ($\sim 4000 \text{ m/s}$) near the edge of the prescribed nucleation patch of the main fault reflecting
407 the high overstress required for initiating the preferred rupture dynamics in our setup. Also, the
408 secondary fault plane features localized supershear episodes ($\sim 3800 \text{ m/s}$). In our model setup,
409 this may be translated into locally high fluid overpressure, and/or reflect the low resolution and
410 1D restriction of the used velocity model. More complex fluid effects have been shown to
411 transition sub-rayleigh to supershear ruptures in fully coupled 2D models by Lin and Zoback
412 (2018).

413 In our preferred model, high slip ($\sim 2 \text{ m}$) occurs in the center of the main fault. We observe
414 a maximum slip of 1.3 m at the secondary fault plane (Figure 7b). In total, the average on-fault
415 slip is 0.32m. Both, Model 1F and Model 2F, feature higher slip than Song and Lee (2019) infer
416 in their static slip inversion. In addition, differences may arise due to different modeling
417 assumptions in terms of fault dimensions and shear moduli. First, Song and Lee (2019) assume a
418 slightly larger shear modulus of $G = 30 \text{ GPa}$ than in our model ($G = 26 \text{ GPa}$). Second, they assume
419 a single fault plane of significantly larger dimensions ($6 \times 5 \text{ km}$) than the faults of our models (see
420 section **Fault reconstruction**). This large fault geometry allows for the possibility of near-surface
421 slip.

422 The orientation of fault slip is modulated by the dynamic source process. The dynamic
423 interaction of the two fault planes induces a moderate thrust-faulting component (rake $\sim 135^\circ -$
424 150°) on the main fault plane, as well as complex time-dependent rake orientations on the
425 secondary fault (see also Figure 7c, 7d). In contrast to Model 2F, the orientations of the final rake
426 angle of Model 1F are distributed homogeneously, on average at 127° . The rake of Model 1F is

427 different from Model 2F due to different dip angles of the main fault which dips at 43° in Model
428 1F. This average rake angle is comparable to the focal mechanism derived by Grigoli et al. (2018).
429 The average on-fault slip is 0.35 m. We observe that, on average, the rupture speed is $v_r \approx 2400$
430 m/s. Reflecting similar dynamic parameters to Model 2F, Model 1F also experiences supershear
431 rupture near the nucleation patch.

432

433 **Waveform comparison for Model 1F and Model 2F**

434 In the following, we analyze the differences between Model 1F and Model 2F in terms of
435 near and far-field ground motion. Hereinafter, all distances from the fault are considered as Joyner-
436 Boore distances (R_{JB} , the shortest distance from a site to the surface projection of fault planes).
437 We compare synthetic waveforms computed for hypothetical (“virtual”) stations located close (~ 4
438 km) and far (>20 km) from the epicenter.

439 Figure 8b shows three-component waveforms at 19 randomly located virtual stations
440 (Figure 8a). We place 10 stations near the epicenter (~ 4 km horizontal distance) to inspect near
441 field seismic waveform characteristics. We filter all synthetic waveforms within the frequency
442 band of 0.1 - 2 Hz using a fourth-order Butterworth filter. Figure 8c depicts all 3-component
443 velocity waveforms. Overall, waveforms of scenarios Model 1F and Model 2F are very similar in
444 this frequency range, but waveforms from Model 1F have systematically higher amplitudes than
445 Model 2F. The most remarkable amplitude differences occur on the EW component for stations
446 004, 008, 009, and 010, which are all located above or close to the faults.

447 At some stations, distinct waveform differences appear (e.g., the NS-component of stations
448 007, 014, 011, and 019). Most of these stations are located on the hanging wall. After five seconds,
449 once the rupture is fully arrested, differences vanish, and the waveforms become comparable for

450 both models. As depicted in Figure 8b, the stations located close to the region where faults overlap
451 in Model 2F show significant differences in seismic wave signatures on the horizontal components.
452 One possible explanation may be that the additional secondary fault defocuses ground motions.

453

454 **Off-fault deformation**

455 Our preferred dynamic earthquake rupture model 2F reveals significant off-fault plastic
456 deformation in the vicinity of geometric fault complexity, similar to scenarios of the 1992 Landers
457 earthquake (Wollherr et al., 2018), the 2016 Kaikoura earthquake (Klinger et al., 2019) and the
458 2019 Ridgecrest earthquake sequence (Taufiqurrahman et al., 2019). Here, significant off-fault
459 plastic deformation (quantified as the scalar quantity η following Ma, 2008 and Wollherr et al.,
460 2019) occurs (i) in the pre-existing damage zone at the fault intersection, (ii) at the dilatational side
461 of the main and the secondary fault as expected from previous theoretical and numerical studies,
462 given the shallow angle of both faults and S_{Hmax} (Templeton and Rice, 2008; Gabriel et al., 2013),
463 and (iii) close to the free-surface (see Figures S4c and S4d).

464 The fault intersection of Model 2F elevates the total off-fault plasticity response
465 regularizing high on-fault stresses while limiting peak slip rates and reducing peak ground motions
466 (Andrews 2005; Dunham et al. 2011a; Gabriel et al., 2013; Roten et al., 2014; Wollherr et al.,
467 2018). When comparing waveforms, we indeed notice overall lower velocity amplitudes compared
468 to Model 1F in the surrounding stations of the fault planes caused by the combined effects of fault
469 complexity and off-fault yielding. Interestingly, the stronger plastic yielding response in model 2F
470 leads to lower variability (not shown here) in ground motions (PGV) (as in Wollherr et al., 2019)
471 even though the fault geometry is more complex.

472

473 **Model 1F and Model 2F surface deformations**

474 Next, we compare the co-seismic surface displacement generated by Model 1F to Model
475 2F (Figure 9a, 9b). We translate the synthetic vertical and horizontal displacements into Line-of-
476 sight (LoS) displacement components.

477 The spatial distribution of the co-seismic surface deformations is noticeably different.
478 Model 1F features higher LoS displacements in southeastern direction relative to the Gokgang
479 Fault (~ 2 km from the bay) compared to Model 2F (~ 5 km from the bay) and generates on
480 average lower negative LoS displacements. Model 1F creates a wider area of uplifted LoS
481 displacements, which resembles an ellipse with a major axis of 6 km and a minor axis of 4.1 km.
482 The most prominent spatial differences are (i) the vertical LoS displacements of Model 1F are
483 slightly migrated to the East relative to the epicenter and (ii) the location of zero displacements in
484 between vertical LoS displacements (in the region of the epicenter) and negative LoS
485 displacements at the eastern-to-southward of the epicenter. Model 2F produces an average of 5 cm
486 subsidence whereas Model 1F only produces 2 cm average subsidence. This can be attributed to
487 Model 1F's more shallow dipping angle. The co-seismic surface displacements of Model 2F
488 compare better than those of Model 1F to InSAR ground deformation inferences of Song and Lee
489 (2019), in terms of the location of the pivot line delimiting positive and negative LoS
490 displacements (~ 4.5 km from the bay).

491 While synthetic (Model 2F) and observed surface displacements significantly differ locally
492 and quantitatively, they reveal qualitatively comparable large-scale features. The following
493 observations are captured by Model 2F: (i) Uplift/easting displacement is observed near the
494 epicenter and (ii) the uplifted area forms an ellipse-like shape with a major axis of ~ 5.6 km and a
495 minor axis of ~ 3.8 km. Correspondingly, Pohang city also experienced subsidence according to

496 field observations (Kang et al., 2019a, Kang et al., 2019b). Additionally, our synthetics also
497 suggest subsidence underneath the bay.

498 Although the contribution of the secondary fault plane is critical to reproduce the inferred
499 non-DC component, comparison of synthetic co-seismic surface displacements of Model 2F with
500 and without the secondary fault (see Figure S5a) suggests that the contribution of the secondary
501 fault plane to the ground displacement is small (Figure S5b), as expected from its small slip
502 contribution. We note that the InSAR data may not be sensitive enough to discriminate between a
503 one and a two-fault plane model.

504

505 **Model 2F validation by regional waveform modeling**

506 Unfortunately, a local seismic network of eight portable seismic stations (Kim et al., 2018)
507 deployed around the EGS site produced saturated (clipped) seismograms. Therefore, we choose to
508 compare synthetic waveforms to regional recordings at five stations surrounding the Pohang EGS
509 site (see Figure 1) at epicentral distances of approximately 70 km.

510 Model 2F compares well to regional low-frequency seismic wave observations (Figure 8c).
511 Synthetic waveforms are calculated using a Green's function database of teleseismic waveforms
512 (Instaseis, Krischer et al., 2017). We translate the dynamic rupture model into a single moment
513 tensor representation following Ulrich et al. (2019a, 2019b). The Green's function database we
514 use is based on the anisotropic Preliminary Reference Earth Model (PREM), and is accurate to a
515 maximum period of 2 s. Synthetic and observed waveforms are filtered using a 0.033 - 0.08 Hz
516 4th order Butterworth filter, equivalent to the frequency band used in the source inversion of
517 Grigoli et al. (2018). The goodness of fit is assessed by the root-mean-square (rms) misfit.

518 Although the synthetic waveforms compare reasonably well to regional recordings, we find
519 that a few synthetic amplitudes are systematically larger than the observed data. We attribute this
520 to the usage of a 1D PREM model, which is more suitable for modeling synthetics at larger
521 azimuthal distance. Additionally, the fact that our simulation returns a slightly higher seismic
522 moment than observed and is not able to capture the full non-DC component of the source may
523 play a role. In particular, the large misfit at Station TJN on the UD and EW component may be
524 attributed to unmodeled site effects. Our synthetics do not differ significantly from the synthetics
525 of Grigoli et al. (2018), derived by full-waveform inversion of the waveforms recorded at stations
526 BUS2, CHJ2, and NAWB. A significant difference is only noticeable on the NS component of
527 station BUS2 (south of the epicenter, Figure 1).

528

529 **Discussion**

530 **The importance of local stresses for rupture dynamics in EGS**

531 The inferences of previous studies vary in terms of stress regimes and maximum horizontal
532 stress orientation around the Pohang EGS site, thereby motivating our systematic numerical
533 experiments as detailed in section **Static and dynamic analysis of initial fault strength and**
534 **stresses** under various loading stress settings. Assuming an Andersonian stress regime, we find
535 that an initial stress state constrained by regional stress inversions is unable to generate the
536 observed thrust-faulting component of the Pohang earthquake. This suggests important local
537 deviations from the regional stress state near the Pohang EGS site. Kim et al. (2017) and Lee et al.
538 (2017) infer the stress orientation at short epicentral distance (< 10 km) from borehole image log
539 data acquired prior to the Pohang earthquake. However, this data is limited to 1 km depth, whereas

540 the Pohang earthquake hypocentral depth is inferred to be deeper, at a depth of 4.27 km. Ellsworth
541 et al. (2019) noted that the in-situ stress state at the Pohang EGS site is transpressional.

542 From our static numerical experiments, we infer that a pure strike-slip stress regime ($s_2 =$
543 s_v) and $S_{Hmax} = 120^\circ$ yield a thrust-faulting component consistent with observations (Figure S2).
544 This finding is corroborated by our dynamic rupture simulations under identical loading (Figure
545 6c, 6d). We also observe that under these conditions spontaneous rupture propagation is favoured.
546 The reverse faulting regime ($s_3 = s_v$) accounting for low $\nu = 0.1$ was also explored. However,
547 such reverse-stress regime, as suggested by Ellsworth et al. (2019), across the entire fault planes
548 does not yield sufficiently high shear tractions on our fault system - and dynamic rupture dies out
549 quickly.

550 Local variations of the stress state around EGS sites, including the Pohang EGS site, have
551 been observed in hydraulic stimulation experiments of crystalline-rock reservoirs (Schoenball et
552 al., 2010), data-driven geomechanical analysis (Ceunot et al., 2006; Hardebeck and Michael, 2006;
553 Martínez-Garzón et al., 2013; Martínez-Garzón et al. 2014; Schoenball et al., 2014) and numerical
554 experiments (Jeanne et al., 2015; Ziegler et al., 2017). Such spatial and temporal stress
555 reorientation is typically a direct response to hydraulic stimulation and fluid injections (Cornet et
556 al., 2007; Schoenball et al., 2010; Schoenball et al., 2013; Ziegler et al., 2017, Liu and Zahradnik,
557 2019). In the geothermal field surrounding the Geysers in California, Martínez-Garzón et al.
558 (2014) found that the stress regime changed from normal-faulting to strike-slip near the injection
559 wells. At the Pohang EGS site, local variations in the stress regime have been inferred from focal
560 mechanisms of microearthquakes before and after the Pohang earthquake. Woo et al. (2019)
561 reported strike-slip faulting north from the hypocenter to strike-slip associated thrust-faulting and
562 pure thrust-faulting components towards the South before the mainshock. After the mainshock

563 occurred, aftershock focal mechanisms were mainly strike-slip in the SW to oblique faulting in the
564 NE (Kim et al., 2020). Changes in the stress orientation and regime near the hypocenter prior to
565 the mainshock could correspond to hydraulic stimulation and fluid injections (Martínez-Garzón et
566 al., 2014; Liu and Zahradnik, 2019). However, the aftershock source characteristics are probably
567 related to co-seismic stress rotation.

568 Based on our analysis of various numerical experiments, we deduce that our models are
569 highly sensitive to variations in the initial stress state, and therefore allow to finely constrain the
570 fault stress loading parameters. For example, a small change in S_{Hmax} may induce a significant
571 change in the modeled focal mechanism. All faults are exposed to the same local stress regime
572 while experiencing varying ratios of shear and normal loading depending on their orientation
573 towards this loading. Even a small change in fault geometry (e.g., in strike, dip, size, and the angle
574 between fault planes) strongly affects the dynamic rupture result (e.g., Yamashita and Umeda,
575 1994; Aochi et al., 2005; Bhat et al., 2007; Ulrich et al., 2019a; van Zelst et al., 2019), as here
576 illustrated when comparing Model 1F and Model 2F. We point out that trade-offs between the
577 inferred stress state and fault geometry can be readily explored if new observations become
578 available.

579 In summary, these observations support our assumption on the loading stress, which is
580 consistent with Ellsworth et al. (2019) in the nucleation region, but differently oriented everywhere
581 else. Complexities in the in-situ stress state are expected in the region where the Pohang earthquake
582 occurred, due to the history of hydraulic stimulations, that is, the EGS operation itself perturbs the
583 local stress conditions in a manner that makes it more difficult to assess the potential seismic
584 hazard implication (that are usually studied in advance and utilize regional stress information).

585

586 **The importance of critically stressed, static and dynamic weak faults and**
587 **overpressurized fluids**

588 Our experiments (Figure 4) emphasize the necessity of assuming overpressurized fluids
589 ($\gamma > 0.37$) and a close to critical stress state when assuming strong frictional weakening on the
590 fault(s). A critically stressed state has been suggested by Ellsworth et al. (2019) by analyzing
591 dipole sonic logging data at the Pohang drilling site. In our preferred Model 2F, we use the ratio
592 of shear over effective normal stress (τ/σ_n) to quantify fault strength, and find 0.54 and 0.59 for
593 the main and secondary fault plane, respectively. This fault strength is close to the assumed steady-
594 state friction coefficient ($f_0 = 0.6$) which indicates that the faults are close to failure prior to
595 rupture nucleation and thus close to critically stressed.

596 In our preferred model both faults are non-optimally oriented with respect to the local stress
597 conditions. The relative prestress ratio R is 0.35 on the main fault and 0.4 on the secondary fault
598 plane, which is less than our assumed $R_0 = 0.8$. According to Andersonian faulting theory, the fault
599 strength is related to its orientation with respect to the regional stress. Here, the main fault plane
600 is oriented at 54° and the secondary fault at 60° relative to the regional maximum compressive
601 stress ($S_{Hmax} = 77^\circ$). Thus, the two-fault system would be considered weak in the classic, static
602 sense.

603 All modeled faults in this study weaken dramatically at co-seismic slip rates while stress
604 drops are limited by the elevated fluid pressure. Besides resembling the dramatic friction decrease
605 observed in laboratory experiments and the theory of thermal weakening processes, previous
606 dynamic rupture studies utilizing rapid velocity weakening using low values of fully weakened
607 friction coefficient (f_w) reproduced rupture complexities, such as rupture reactivation and pulse-
608 like ruptures, without assuming small-scale heterogeneities (Ulrich et al., 2019a).

609 In our simulation, we use a fluid pressure ratio of 0.5 which corresponds to a reduction of
610 the normal stress of approximately 14.3 MPa compared to a hydrostatic state. The reduction in
611 effective normal stress mechanically lowers the static strength of faults. Our assumption of high
612 fluid pressure may relate to various episodes of drilling mud loss on 30-31 October 2015 at 3800
613 m depth suggesting an increase of fluid pressure on the order of 20 MPa around the borehole, and
614 the fluid injection operations (Ellsworth et al., 2019; Korean Government Commission, 2019).

615

616 **The importance of fault interaction for the dynamic rupture process and** 617 **faulting mechanism**

618 In our preferred model, the secondary fault is only partially ruptured during the Pohang
619 earthquake. Strong variations in slip rate associated with dynamic rupture complexity across the
620 two faults planes and their interaction, spontaneous rupture arrest and the asymmetrically
621 accumulated fault slip on the main and secondary fault plane, could potentially favor dynamic and
622 static Coulomb stress transfers enabling a later activation of the unruptured area of the secondary
623 fault. The largest aftershock that occurred less than three hours after the mainshock at 650 m
624 epicentral distance to the northwest with respect to the mainshock may have occurred in such an
625 unruptured area on the secondary fault.

626 In our model, complex shear faulting across two fault planes induces a non-DC component,
627 which is, nevertheless, considerably smaller (14%) compared to the CLVD component inferred by
628 Grigoli et al. (2018). Additional factors not considered in this study may contribute to an apparent
629 non-DC component, such as strong deviations from fault planarity (larger scale curvature and
630 small-scale roughness, e.g., Bydlon and Dunham, 2015; Shi and Day, 2013; Ulrich and Gabriel,
631 2017; Mai et al., 2018), stronger heterogeneities in fault stress and strength (Ripperger et al., 2008)

632 and 3D subsurface structure (e.g., Pelties et al., 2015) increasing rupture complexity, as well as
633 incorporating tensile faulting, poroelastic rheology, and source or propagation anisotropy (Julian,
634 1998; Boitz et al., 2018). The CLVD contribution may also increase when assuming a larger
635 number of faults. While the limited data available does not suggest rupture of additional fault
636 planes, stochastically distributed and dynamically activated fracture networks (e.g., Okubo et al.
637 2019; Anger and Gabriel, 2019) around the main fault are expected given the on-going stimulation
638 operation.

639

640 **Importance of dense seismic monitoring during EGS projects**

641 The complex interaction of local stress loading and fault strength conditions, rupture
642 dynamics and fault interaction on multiple fault segments presented here highlights the importance
643 of a dense local seismic network within the operational areas for monitoring and analyzing
644 microseismicity before, during, and after EGS operation, to thereby mitigate the potential seismic
645 hazard. Pre-EGS stimulation seismic monitoring is needed to define the ‘unperturbed state’ of the
646 system (the rock volume to be stimulated) and for characterizing potentially unmapped fault(s)
647 that may interact during cascading rupture; such seismic monitoring may be accompanied by
648 detailed borehole logging to assess the local stress state prior to stimulation.

649 During the stimulation and operational phase, a dense seismic monitoring network is also
650 needed to facilitate high-precision and high-fidelity seismic source studies. In conjunction with
651 detailed operational fluid-injection parameters, the reservoir stress state and its susceptibility for
652 generating earthquakes can be assessed (Galis et al., 2017; Kwiatek et al., 2019). In fact, the
653 available recordings of the operational monitoring seismic network near the Pohang EGS site were
654 saturated (clipped) by the unexpected high magnitude earthquake, thus accelerometers would be

655 useful as complementary instruments in EGS monitoring networks. In addition, the rise of
656 Distributed Acoustic Sensing (DAS) opens new opportunities as an additional seismic monitoring
657 network especially for EGS that is located in urban areas (Zhan, 2019).

658 Our study suggests that fully physics-based numerical simulations prior, during and after
659 an EGS project may be useful to not only gain a first-order understanding of potential effects and
660 consequences of the EGS experiments (e.g., risk-prone area as reflected by peak ground motions
661 (PGVs, Figure S6)), but also to optimally design the seismic monitoring network to ensure that all
662 vital data are collected as needed for future monitoring and mitigation purposes.

663

664 **Conclusions**

665 A guided fault reconstruction approach that clusters spatio-temporal aftershock locations
666 accounting for their uncertainty is applied to create a two fault planes dynamic rupture model
667 which reproduces key characteristics of the Pohang earthquake. Rupture complexity is arising from
668 the dynamic interaction of two failing fault planes with shallow intersection angles.

669 Static Mohr-Coulomb failure analysis and 180 numerical simulations demonstrate that the
670 regional loading stress is unable to generate dynamic rupture consistent with the observed faulting
671 style. Resolving the regional tectonic stress field onto one fault of a geometry as suggested by
672 Korean Government Commission (2019), Ellsworth et al. (2019), and Woo et al. (2019) or onto
673 the reconstructed two fault planes leads inevitable to pure strike-slip faulting, in stark contrast to
674 the observed thrust-faulting mechanism. Instead, local stress variation relative to regional stress
675 orientation is needed to generate oblique faulting. We conclude that regional-stress orientation
676 may be misleading when assessing propensity for failure; this has important implications for
677 seismic hazard assessment. Also, overpressurized pore fluids, non-optimally oriented and

678 dynamically weak faults and a close to critical local stress state play major roles for our dynamic
679 rupture models of the Pohang earthquake. Such factors may be assessed when planning and
680 conducting EGS-type experiments, explorations, and operations.

681 Our dynamic rupture simulations reveal dynamic triggering from the main fault plane to
682 the secondary fault plane without direct rupture branching but via “rupture jumping”. The
683 preferred two fault plane simulation compares well to regional observed data such as moment
684 release and far-field seismic waveforms. The single fault plane model, on the other hand, is unable
685 to reproduce the observed non-DC focal mechanisms and surface displacement distributions due
686 to simplicity of the dynamic rupture process and a shallower dip angle, respectively. Dynamic fault
687 interaction, amplified by rapid stress changes due to seismic waves reverberating between the two
688 fault planes, are needed to reproduce observations of a strong CLVD component. However, two
689 simultaneously breaking fault planes cannot fully explain the observed source complexity.

690 We demonstrate the maturity and feasibility of high-resolution 3D modeling of rupture
691 dynamics and seismic wave propagation accounting for the complexity of EGS environments and
692 constrained by few observational parameters shedding light on the dynamics of induced and
693 triggered earthquakes. More sophisticated 3D models, fully coupling dynamic earthquake rupture
694 and seismic wave propagation with co-seismic and quasi-static fluid effects, such as poroelasticity,
695 thermal pressurization, pore pressure diffusion, and considering the geometric complexity of
696 networks of fractures and non-planar faults, may allow in future to capture the full physical
697 complexity of nucleation and dynamics of induced earthquakes.

698 In the near future, such physics-based approaches may be synergistically integrated with
699 near-field seismic monitoring before, during, and after EGS operation, thus complementing traffic
700 light systems for hazard and risk mitigation (Bommer et al., 2006; Mignan et al., 2015).

701

702 **Data and resources**

703 The open-source software package SeisSol can be downloaded in github repository
704 (<https://github.com/SeisSol/SeisSol>). All regional waveforms used in this study were
705 downloaded from Incorporated Research Institutions for Seismology (IRIS; <https://www.iris.edu>
706 (last accessed February 2020)) data management system using FDSN client. PREM anisotropic 2
707 s can be downloaded in the IRIS data services products (<http://ds.iris.edu/ds/products/syngine/>
708 (last accessed February 2020)). The supplemental for this article provides additional figures, a
709 table, all parameters used for the preferred Model 2F, and a video mentioned in the article. All
710 parameters used for the preferred Model 2F are also available at
711 (https://drive.google.com/open?id=1nm3HZ_YOD-j8t_YatTFfs9prVKplEEExj).

712

713 **Acknowledgments**

714 We thank Xing Li and Prof. Sigurjón Jónsson for the discussions regarding surface deformations
715 using InSAR. We also thank Prof. Guy Ouillon for providing us the raw code of ACLUD. We
716 acknowledge Dr. Seok Goo Song and Prof. Hoonyol Lee for sharing the processed InSAR images
717 and discussions about inversion parameters. Computing resources were provided by King
718 Abdullah University of Science and Technology, Thuwal, Saudi Arabia (KAUST, project k1219
719 and k1343 on Shaheen II). The work presented in this paper was supported by The KAUST grants
720 (FRAGEN, ORS-2017-CRG6 3389.02), URF/1/3389-01-01, and BAS/1339-01-01. J.A.L-C has
721 also received funding from the European Union's Horizon 2020 research and innovation
722 programme under the Marie Skłodowska-Curie grant agreement N° 754446 and UGR Research

723 and Knowledge Transfer Found – Athenea3i; and by the Deutsche Forschungsgemeinschaft (DFG,
724 German Research Foundation) – Projektnummer (407141557). TU and A.-A.G acknowledge
725 additional support by the European Union’s Horizon 2020 research and innovation program
726 (ChEESE, grant no. 823844) and the European Research Council (TEAR, ERC Starting grant no.
727 852992). Part of the analysis was implemented using ObsPy (Beyreuther et al., 2010). Figures
728 were prepared using Paraview (Ahrens et al., 2005), Generic Mapping Tools (Wessel et al., 2013)
729 and Matplotlib (Hunter, 2007)

730

731 **References**

732 Ahrens, J., B. Geveci, and C. Law, 2005, ParaView: An end-user tool for large-data
733 visualization, in Visualization Handbook, Elsevier Inc., 717–731.

734 Andrews, D. J., 2005, Rupture dynamics with energy loss outside the slip zone, *J. Geophys. Res.*,
735 110, no. B1, B01307, doi: 10.1029/2004JB003191.

736 Anger, S. and A.-A Gabriel (2019). Dynamic earthquake rupture across complex 3D
737 fracture networks. S55E-0444 presented at 2019 Fall Meeting, AGU, San Francisco, CA, 9-
738 13 Dec.

739 Aochi, H., and R. Madariaga, 2003, The 1999 Izmit, Turkey, earthquake: Nonplanar fault
740 structure, dynamic rupture process, and strong ground motion, *Bull. Seismol. Soc. Am.*, 93,
741 no. 3, 1249–1266, doi: 10.1785/0120020167.

742 Aochi, H., O. Scotti, and C. Berge-Thierry, 2005, Dynamic transfer of rupture across differently
743 oriented segments in a complex 3-D fault system, *Geophys. Res. Lett.*, 32, no. 21, L21304,

744 doi: 10.1029/2005GL024158.

745 Bauer, A., Scheipl, F., Küchenhoff, H., and Gabriel, A.-A. (2018). An introduction to
746 semiparametric function-on-scalar regression. *Statistical Modelling*, 18(3–4), 346–364.
747 <https://doi.org/10.1177/1471082X17748034>.

748 Beyreuther, M., R. Barsch, L. Krischer, T. Megies, Y. Behr, and J. Wassermann, 2010, ObsPy: A
749 python toolbox for seismology, *Seismol. Res. Lett.*, 81, no. 3, 530–533, doi:
750 10.1785/gssrl.81.3.530.

751 Bhat, H. S., M. Olives, R. Dmowska, and J. R. Rice, 2007, Role of fault branches in earthquake
752 rupture dynamics, *J. Geophys. Res.*, 112, no. B11, B11309, doi: 10.1029/2007JB005027.

753 Boitz, N., A. Reshetnikov, and S. A. Shapiro, 2018, Visualizing effects of anisotropy on seismic
754 moments and their potency-tensor isotropic equivalent, *Geophysics*, 83, no. 3, C85–C97,
755 doi: 10.1190/geo2017-0442.1.

756 Bommer, J.J., Oates, S., Cepeda, J.M., Lindholm, C., Bird, J., Torres, R., Marroquín, G. and
757 Rivas, J., 2006. Control of hazard due to seismicity induced by a hot fractured rock
758 geothermal project. *Engineering Geology*, 83(4), pp.287-306.

759 Breuer, A., A. Heinecke, and M. Bader, 2016, Petascale Local Time Stepping for the ADER-DG
760 Finite Element Method, in *Proceedings - 2016 IEEE 30th International Parallel and
761 Distributed Processing Symposium, IPDPS 2016, Institute of Electrical and Electronics
762 Engineers Inc.*, 854–863.

763 Breuer, A., A. Heinecke, S. Rettenberger, M. Bader, A.-A. Gabriel, and C. Pelties, 2014,

- 764 Sustained Petascale Performance of Seismic Simulations with SeisSol on SuperMUC, 1–18.
- 765 Bydlon, S. A., and E. M. Dunham, 2015, Rupture dynamics and ground motions from
766 earthquakes in 2-D heterogeneous media, *Geophys. Res. Lett.*, 42, no. 6, 1701–1709, doi:
767 10.1002/2014GL062982.
- 768 Cappa, F., and J. Rutqvist, 2012, Seismic rupture and ground accelerations induced by CO₂
769 injection in the shallow crust, *Geophys. J. Int.*, 190, no. 3, 1784–1789, doi: 10.1111/j.1365-
770 246X.2012.05606.x.
- 771 Chang, K. W., H. Yoon, Y. Kim, and M. Y. Lee, 2020, Operational and geological controls of
772 coupled poroelastic stressing and pore-pressure accumulation along faults: Induced
773 earthquakes in Pohang, South Korea, *Sci. Rep.*, 10, no. 1, 2073, doi: 10.1038/s41598-020-
774 58881-z.
- 775 Cheng, Y., and X. Chen, 2018, Characteristics of seismicity inside and outside the salton sea
776 geothermal field, *Bull. Seismol. Soc. Am.*, 108, no. 4, 1877–1888, doi:
777 10.1785/0120170311.
- 778 Choi, J. H., K. Ko, Y. S. Gihn, C. S. Cho, H. Lee, S. G. Song, E. S. Bang, H. J. Lee, H. K. Bae,
779 S. W. Kim et al., 2019, Surface deformations and rupture processes associated with the
780 2017 Mw 5.4 Pohang, Korea, earthquake, *Bull. Seismol. Soc. Am.*, 109, no. 2, 756–769,
781 doi: 10.1785/0120180167.
- 782 Cornet, F.H., T. Bérard, and S. Bourouis, 2007. How close to failure is a granite rock mass at a 5
783 km depth?. *International Journal of Rock Mechanics and Mining Sciences*, 44(1), pp.47-66.

- 784 Cuenot, N., J. Charléty, L. Dorbath, and H. Haessler, 2006, Faulting mechanisms and stress
785 regime at the European HDR site of Soultz-sous-Forêts, France, *Geothermics*, 35, nos. 5–6,
786 561–575, doi: 10.1016/j.geothermics.2006.11.007.
- 787 Dieterich, J. H., K. B. Richards-Dinger, and K. A. Kroll, 2015, Modeling injection-induced
788 seismicity with the physics-based earthquake simulator RSQSim, *Seismol. Res. Lett.*, 86,
789 no. 4, 1102–1109, doi: 10.1785/0220150057.
- 790 Duan, B., 2016, Spontaneous rupture on natural fractures and seismic radiation during hydraulic
791 fracturing treatments, *Geophys. Res. Lett.*, 43, no. 14, 7451–7458, doi:
792 10.1002/2016GL069083.
- 793 Dumbser, M., and M. Käser, 2006, An arbitrary high-order discontinuous Galerkin method for
794 elastic waves on unstructured meshes - II. The three-dimensional isotropic case, *Geophys. J.
795 Int.*, 167, no. 1, 319–336, doi: 10.1111/j.1365-246X.2006.03120.x.
- 796 Dunham, E. M., D. Belanger, L. Cong, and J. E. Kozdon, 2011a, Earthquake ruptures with
797 strongly rate-weakening friction and off-fault plasticity, part 1: Planar faults, *Bull. Seismol.
798 Soc. Am.*, 101, no. 5, 2296–2307, doi: 10.1785/0120100075.
- 799 Dunham, E. M., D. Belanger, L. Cong, and J. E. Kozdon, 2011b, Earthquake ruptures with
800 strongly rate-weakening friction and off-fault plasticity, part 2: Nonplanar faults, *Bull.
801 Seismol. Soc. Am.*, 101, no. 5, 2308–2322, doi: 10.1785/0120100076.
- 802 Ellsworth, W. L., D. Giardini, J. Townend, S. Ge, and T. Shimamoto, 2019, Triggering of the
803 Pohang, Korea, Earthquake (Mw 5.5) by enhanced geothermal system stimulation,
804 *Seismological Society of America*, 1844–1858.

- 805 Emerson paradigm holding, 2018, GoCad: A computer aided design program for geological
806 applications.
- 807 Gabriel, A.-A., J.-P. Ampuero, L. A. Dalguer, and P. M. Mai, 2013, Source properties of
808 dynamic rupture pulses with off-fault plasticity, *J. Geophys. Res. Solid Earth*, 118, no. 8,
809 4117–4126, doi: 10.1002/jgrb.50213.
- 810 Galis, M., J. P. Ampuero, P. M. Mai, and F. Cappa, 2017, Induced seismicity provides insight
811 into why earthquake ruptures stop, *Sci. Adv.*, 3, no. 12, doi: 10.1126/sciadv.aap7528.
- 812 Gallovič, F., Valentová, L., Ampuero, J.-P., and Gabriel, A.-A. , 2019a. Bayesian dynamic finite-
813 fault inversion: 1. Method and synthetic test. *J. Geophys. Res.*, 124, 6949– 6969.
814 <https://doi.org/10.1029/2019JB017510>
- 815 Gallovič, F., Valentová, L., Ampuero, J.-P., and Gabriel, A.-A., 2019b. Bayesian Dynamic
816 Finite-Fault Inversion: 2. Application to the 2016 Mw6.2 Amatrice, Italy, Earthquake, *J.*
817 *Geophys. Res.*, doi:10.1029/2019JB017512.
- 818 Garagash, D. I., and L. N. Germanovich, 2012, Nucleation and arrest of dynamic slip on a
819 pressurized fault, *J. Geophys. Res. B Solid Earth*, 117, no. 10, doi: 10.1029/2012JB009209.
- 820 Grigoli, F., S. Cesca, A. P. Rinaldi, A. Manconi, J. A. López-Comino, J. F. Clinton, R.
821 Westaway, C. Cauzzi, T. Dahm, and S. Wiemer, 2018, The November 2017 M w 5.5
822 Pohang earthquake: A possible case of induced seismicity in South Korea, *Science* (80-.),
823 360, no. 6392, 1003–1006, doi: 10.1126/science.aat2010.
- 824 Happ, C., Scheipl, F., A.-A. Gabriel, S. Greven, 2019, A general framework for multivariate

- 825 functional principal component analysis of amplitude and phase variation. *Stat.* 2019;
826 8:e220. <https://doi.org/10.1002/sta4.220>
- 827 Hardebeck, J. L., and A. J. Michael, 2006, Damped regional-scale stress inversions:
828 Methodology and examples for southern California and the Coalinga aftershock sequence,
829 *J. Geophys. Res. Solid Earth*, 111, no. B11, doi: 10.1029/2005JB004144.
- 830 Harris, R. A., M. Barall, B. Aagaard, S. Ma, D. Roten, K. Olsen, B. Duan, D. Lie, B. Luo, K. Bai
831 et al., 2018, A suite of exercises for verifying dynamic earthquake rupture codes, *Seismol.*
832 *Res. Lett.*, 89, no. 3, 1146–1162, doi: 10.1785/0220170222.
- 833 Harris, R. A., M. Barall, D. J. Andrews, B. Duan, S. Ma, E. M. Dunham, A.-A. Gabriel, Y.
834 Kaneko, Y. Kase, B. T. Aagaard et al., 2011, Verifying a Computational Method for
835 Predicting Extreme Ground Motion, *Seismol. Res. Lett.*, 82, no. 5, 638–644, doi:
836 10.1785/gssrl.82.5.638.
- 837 Heidbach, O. M. Rajabi, X. Cui, K. Fuchs, B. Muller, J. Reinecker, K. Reiter, M. Tingay, F.
838 Wenzel, F. Xie, et al., 2018, The World Stress Map database release 2016: Crustal stress
839 pattern across scales, Elsevier B.V., 484–498.
- 840 Heinecke, A., A. Breuer, S. Retenberger, M. Bader, A.-A. Gabriel, C. Pelties, A. Bode, W.
841 Barth, X. Liao, K. Vaidyanathan, et al., 2014, Petascale High Order Dynamic Rupture
842 Earthquake Simulations on Heterogeneous Supercomputers, in International Conference for
843 High Performance Computing, Networking, Storage and Analysis, SC, IEEE Computer
844 Society, 3–14.
- 845 Hirata, T., 1989, Fractal dimension of fault systems in Japan: Fractal structure in rock fracture

846 geometry at various scales, *Pure Appl. Geophys. PAGEOPH*, 131, nos. 1–2, 157–170, doi:

847 10.1007/BF00874485.

848 Hofmann, H., G. Zimmermann, M. Farkas, E. Huenges, A. Zang, M. Leonhardt, G. Kwiatek, P.

849 Martinez-Garzon, M. Bohnhoff, K. B. Min et al., 2019, First field application of cyclic soft

850 stimulation at the Pohang Enhanced Geothermal System site in Korea, *Geophys. J. Int.*

851 (2019) 217, 926–949

852 Hunter, J. D., 2007, Matplotlib: A 2D graphics environment, *Comput. Sci. Eng.*, 9, no. 3, 99–

853 104, doi: 10.1109/MCSE.2007.55.

854 Jeanne, P., J. Rutqvist, P. F. Dobson, J. Garcia, M. Walters, C. Hartline, and A. Borgia, 2015,

855 Geomechanical simulation of the stress tensor rotation caused by injection of cold water in a

856 deep geothermal reservoir, *J. Geophys. Res. Solid Earth*, 120, no. 12, 8422–8438, doi:

857 10.1002/2015JB012414.

858 Jin, L., and M. D. Zoback, 2018, Fully Dynamic Spontaneous Rupture Due to Quasi-Static Pore

859 Pressure and Poroelastic Effects: An Implicit Nonlinear Computational Model of Fluid-

860 Induced Seismic Events, *J. Geophys. Res. Solid Earth*, 123, no. 11, 9430–9468, doi:

861 10.1029/2018JB015669.

862 Julian, B. R., A. D. Miller, and G. R. Foulger, 1998, Non-double-couple earthquakes 1. Theory,

863 *Rev. Geophys.*, 36, no. 4, 525–549, doi: 10.1029/98RG00716.

864 Kang, S., B. Kim, S. Bae, H. Lee, and M. Kim, 2019a, Earthquake-Induced Ground

865 Deformations in the Low-Seismicity Region: A Case of the 2017 M5.4 Pohang, South

866 Korea, *Earthquake, Earthq. Spectra*, 35, no. 3, 1235–1260, doi: 10.1193/062318EQS160M.

- 867 Kang, S., B. Kim, H. Cho, J. Lee, K. Kim, S. Bae, and C. Sun, 2019b, Ground-Motion
868 Amplifications in Small-Size Hills: Case Study of Gokgang-ri, South Korea, during the
869 2017 ML 5.4 Pohang Earthquake Sequence, *Bull. Seismol. Soc. Am.*, 109, no. 6, 2626–
870 2643, doi: 10.1785/0120190064.
- 871 Käser, M., and M. Dumbser, 2006, An arbitrary high-order discontinuous Galerkin method for
872 elastic waves on unstructured meshes - I. The two-dimensional isotropic case with external
873 source terms, *Geophys. J. Int.*, 166, no. 2, 855–877, doi: 10.1111/j.1365-
874 246X.2006.03051.x.
- 875 Kim, K. H., J. H. Ree, Y. H. Kim, S. Kim, S. Y. Kang, and W. Seo, 2018, Assessing whether the
876 2017 Mw5.4 Pohang earthquake in South Korea was an induced event, *Science (80-.)*, 360,
877 no. 6392, 1007–1009, doi: 10.1126/science.aat6081.
- 878 Kim, K. H., W. Seo, J. Han, J. Kwon, S. Y. Kang, J. H. Ree, S. Kim, and K. Liu, 2020, The 2017
879 ML 5.4 Pohang earthquake sequence, Korea, recorded by a dense seismic network,
880 *Tectonophysics*, 774, doi: 10.1016/j.tecto.2019.228306.
- 881 Kim, H., L. Xie, K. B. Min, S. Bae, and O. Stephansson, 2017, Integrated In Situ Stress
882 Estimation by Hydraulic Fracturing, Borehole Observations and Numerical Analysis at the
883 EXP-1 Borehole in Pohang, Korea, *Rock Mech. Rock Eng.*, 50, no. 12, 3141–3155, doi:
884 10.1007/s00603-017-1284-1.
- 885 Klinger, Y., K. Okubo, A. Vallage, J. Champenois, A. Delorme, E. Rougier, Z. Lei, E. E. Knight,
886 A. Munjiza, C. Satriano, et al., 2018, Earthquake Damage Patterns Resolve Complex
887 Rupture Processes, *Geophys. Res. Lett.*, 45, no. 19, 10,279-10,287, doi:

- 888 10.1029/2018GL078842.
- 889 Korean Government Commission, 2019, Summary Report of the Korean Government
890 Commission on Relations between the 2017 Pohang Earthquake and EGS Project.
- 891 Krischer, L., A. R. Hutko, M. Van Driel, S. Stähler, M. Bahavar, C. Trabant, and T. Nissen-
892 Meyer, 2017, On-demand custom broadband synthetic seismograms, *Seismol. Res. Lett.*,
893 88, no. 4, 1127–1140, doi: 10.1785/0220160210.
- 894 Kroll, K. A., K. B. Richards-Dinger, and J. H. Dieterich, 2017, Sensitivity of Induced Seismic
895 Sequences to Rate-and-State Frictional Processes, *J. Geophys. Res. Solid Earth*, 122, no. 12,
896 10,207–10,219, doi: 10.1002/2017JB014841.
- 897 Kwiatek, G., T. Saarno, T. Ader, F. Bluemle, M. Bohnhoff, M. Chendorain, G. Dresen, P.
898 Heikkinen, I. Kukkonen, P. Leary et al., 2019, Controlling fluid-induced seismicity during a
899 6.1-km-deep geothermal stimulation in Finland, *Sci. Adv.*, 5, no. 5, eaav7224, doi:
900 10.1126/sciadv.aav7224.
- 901 Kyriakopoulos, C., D. D. Oglesby, T. K. Rockwell, A. J. Meltzner, M. Barall, J. M. Fletcher, and
902 D. Tulanowski, 2019, Dynamic Rupture Scenarios in the Brawley Seismic Zone, Salton
903 Trough, Southern California, *J. Geophys. Res. Solid Earth*, 124, no. 4, 3680–3707, doi:
904 10.1029/2018JB016795.
- 905 de la Puente, J., J.-P. Ampuero, and M. Käser, 2009, Dynamic rupture modeling on unstructured
906 meshes using a discontinuous Galerkin method, *J. Geophys. Res.*, 114, no. B10, B10302,
907 doi: 10.1029/2008JB006271.

- 908 Lee, K. K., W. L. Ellsworth, D. Giardini, J. Townend, S. Ge, T. Shimamoto, I. W. Yeo, T. S.
909 Kang, J. Rhie, D. G. Sheen et al., 2019, Managing injection-induced seismic risks, *Science*,
910 364, no. 6442, 730–732, doi: 10.1126/science.aax1878.
- 911 Lee, J., T. K. Hong, and C. Chang, 2017, Crustal stress field perturbations in the continental
912 margin around the Korean Peninsula and Japanese islands, *Tectonophysics*, 718, 140–149,
913 doi: 10.1016/j.tecto.2017.08.003.
- 914 Lee, H., Y. J. Shinn, S. H. Ong, S. W. Woo, K. G. Park, T. J. Lee, and S. W. Moon, 2017, Fault
915 reactivation potential of an offshore CO₂ storage site, Pohang Basin, South Korea, *J. Pet.*
916 *Sci. Eng.*, 152, 427–442, doi: 10.1016/j.petrol.2017.03.014.
- 917 Liu, J. and Zahradník, J., The 2019 MW 5.7 Changning earthquake, Sichuan Basin, China—a
918 shallow doublet with different faulting styles. *Geophys. Res. Lett.*, p.e2019GL085408.
- 919 Ma, S., 2008, A physical model for widespread near-surface and fault zone damage induced by
920 earthquakes. *Geochemistry, Geophysics, Geosystems*, 9(11).
- 921 Mai, P. M., M. Galis, K. K. S. Thingbaijam, J. C. Vyas, and E. M. Dunham, 2018, Accounting
922 for Fault Roughness in Pseudo-Dynamic Ground-Motion Simulations, Birkhäuser, Cham,
923 95–126.
- 924 Martínez-Garzón, P., M. Bohnhoff, G. Kwiatek, and G. Dresen, 2013, Stress tensor changes
925 related to fluid injection at The Geysers geothermal field, California, *Geophys. Res. Lett.*,
926 40, no. 11, 2596–2601, doi: 10.1002/grl.50438.
- 927 Martínez-Garzón, P., G. Kwiatek, H. Sone, M. Bohnhoff, G. Dresen, and C. Hartline, 2014,

- 928 Spatiotemporal changes, faulting regimes, and source parameters of induced seismicity: A
929 case study from The Geysers geothermal field, *J. Geophys. Res. Solid Earth*, 119, no. 11,
930 8378–8396, doi: 10.1002/2014JB011385.
- 931 McGarr, A., 2014, Maximum magnitude earthquakes induced by fluid injection, *J. Geophys.*
932 *Res. Solid Earth*, 119, no. 2, 1008–1019, doi: 10.1002/2013JB010597.
- 933 Mignan, A., Landtwing, D., Kästli, P., Mena, B. and Wiemer, S., 2015. Induced seismicity risk
934 analysis of the 2006 Basel, Switzerland, Enhanced Geothermal System project: Influence of
935 uncertainties on risk mitigation. *Geothermics*, 53, pp.133-146.
- 936 Okubo, K., H. S. Bhat, E. Rougier, S. Marty, A. Schubnel, Z. Lei, E. E. Knight, and Y. Klinger,
937 2019, Dynamics, Radiation, and Overall Energy Budget of Earthquake Rupture With
938 Coseismic Off-Fault Damage, *J. Geophys. Res. Solid Earth*, 124, no. 11, 11771–11801, doi:
939 10.1029/2019JB017304.
- 940 Pelties, C., A.-A. Gabriel, and J.-P. Ampuero, 2014, Verification of an ADER-DG method for
941 complex dynamic rupture problems, *Geosci. Model Dev.*, 7, no. 3, 847–866, doi:
942 10.5194/gmd-7-847-2014 and *Geoscientific Model Development Discussions*, 6(4), 5981--
943 6034, doi:10.5194/gmdd-6-5981-2013.
- 944 Pelties, C., Y. Huang, and J. P. Ampuero, 2015, Pulse-Like Rupture Induced by Three-
945 Dimensional Fault Zone Flower Structures, *Pure Appl. Geophys.*, 172, no. 5, 1229–1241,
946 doi: 10.1007/s00024-014-0881-0.
- 947 Pelties, C., J. de la Puente, J.-P. Ampuero, G. B. Brietzke, and M. Käser, 2012, Three-
948 dimensional dynamic rupture simulation with a high-order discontinuous Galerkin method

- 949 on unstructured tetrahedral meshes, *J. Geophys. Res. Solid Earth*, 117, no. B2, n/a-n/a, doi:
950 10.1029/2011JB008857.
- 951 Peyrat, S., K. Olsen, and R. Madariaga, 2001, Dynamic modeling of the 1992 Landers
952 earthquake, *J. Geophys. Res. Solid Earth*, 106, no. B11, 26467–26482, doi:
953 10.1029/2001jb000205.
- 954 Rettenberger, S., O. Meister, M. Bader, and A. A. Gabriely, 2016, ASAGI - A parallel server for
955 adaptive geoinformation, in *ACM International Conference Proceeding Series*, Association
956 for Computing Machinery.
- 957 Richards-Dinger, K., and J. H. Dieterich, 2012, RSQSim earthquake simulator, *Seismol. Res.*
958 *Lett.*, 83, no. 6, 983–990, doi: 10.1785/0220120105.
- 959 Ripperger, J., Mai, P.M. and Ampuero, J.P., 2008. Variability of near-field ground motion from
960 dynamic earthquake rupture simulations. *Bulletin of the seismological society of America*,
961 98(3), pp.1207-1228.
- 962 Roten, D., K. B. Olsen, S. M. Day, Y. Cui, and D. Fäh, 2014, Expected seismic shaking in Los
963 Angeles reduced by San Andreas fault zone plasticity, *Geophys. Res. Lett.*, 41, no. 8, 2769–
964 2777, doi: 10.1002/2014GL059411.
- 965 Schoenball, M., L. Dorbath, E. Gaucher, J. F. Wellmann, and T. Kohl, 2014, Change of stress
966 regime during geothermal reservoir stimulation, *Geophys. Res. Lett.*, 41, no. 4, 1163–1170,
967 doi: 10.1002/2013GL058514.
- 968 Schoenball, M., T. M. Müller, B. I. R. Müller, and O. Heidbach, 2010, Fluid-induced

- 969 microseismicity in pre-stressed rock masses, *Geophys. J. Int.*, 180, no. 2, 813–819, doi:
970 10.1111/j.1365-246X.2009.04443.x.
- 971 Shi, Z., and S. M. Day, 2013, Rupture dynamics and ground motion from 3-D rough-fault
972 simulations, *J. Geophys. Res. Solid Earth*, 118, no. 3, 1122–1141, doi: 10.1002/jgrb.50094.
- 973 Simmetrix Inc, 2017, SimModeler: Simulation modeling suite 14.0 documentation (Tech. Rep.).
- 974 Soh, I., C. Chang, J. Lee, T.-K. Hong, and E.-S. Park, 2018, Tectonic stress orientations and
975 magnitudes, and friction of faults, deduced from earthquake focal mechanism inversions
976 over the Korean Peninsula, *Geophys. J. Int.*, 213, no. 2, 1360–1373, doi:
977 10.1093/gji/ggy061.
- 978 Song, S. G., and H. Lee, 2019, Static slip model of the 2017 M w 5.4 Pohang, South Korea,
979 earthquake constrained by the InSAR data, *Seismol. Res. Lett.*, 90, no. 1, 140–148, doi:
980 10.1785/0220180156.
- 981 Di Toro, G., R. Han, T. Hirose, N. De Paola, S. Nielsen, K. Mizoguchi, F. Ferri, M. Cocco, and
982 T. Shimamoto, 2011, Fault lubrication during earthquakes, *Nature*, 471, no. 7339, 494–499,
983 doi: 10.1038/nature09838.
- 984 Taufiqurrahman, T., A.-A. Gabriel, B. Li, D. Li, S. A. Wirp, T. Ulrich, K. H. Palgunadi, A.
985 Verdecchia, S. Carena, and Z. K. Mildon, 2019, High-resolution integrated dynamic rupture
986 modeling of the 2019 M6. 4 Searles Valley and M7. 1 Ridgecrest earthquakes. S31G-0487
987 presented at 2019 Fall Meeting, AGU, San Francisco, CA, 9-13 Dec.
- 988 Templeton, E.L. and Rice, J.R., 2008. Off-fault plasticity and earthquake rupture dynamics: 1.

- 989 Dry materials or neglect of fluid pressure changes. *J. Geophys. Res.: Solid Earth*, 113(B9).
- 990 Ulrich, T., and A.-A. Gabriel, 2017, 3D fault curvature and fractal roughness: Insights for
991 rupture dynamics and ground motions using a Discontinuous Galerkin method. In EGU
992 General Assembly Conference Abstract, Vol. 19, Vienna, Austria, pp. 18689.
- 993 Ulrich, T., A. A. Gabriel, J. P. Ampuero, and W. Xu, 2019a, Dynamic viability of the 2016 Mw
994 7.8 Kaikōura earthquake cascade on weak crustal faults, *Nat. Commun.*, 10, no. 1, doi:
995 10.1038/s41467-019-09125-w.
- 996 Ulrich, T., S. Vater, E. H. Madden, J. Behrens, Y. van Dinther, I. van Zelst, E. J. Fielding, C.
997 Liang, and A. A. Gabriel, 2019b, Coupled, Physics-Based Modeling Reveals Earthquake
998 Displacements are Critical to the 2018 Palu, Sulawesi Tsunami, *Pure Appl. Geophys.*, 176,
999 no. 10, 4069–4109, doi: 10.1007/s00024-019-02290-5.
- 1000 Uphoff, C. and Bader, M., 2016, July. Generating high performance matrix kernels for
1001 earthquake simulations with viscoelastic attenuation. In 2016 International Conference on
1002 High Performance Computing and Simulation (HPCS) (pp. 908-916). IEEE.
- 1003 Uphoff, C., S. Rettenberger, M. Bader, E. H. Madden, T. Ulrich, S. Wollherr, and A.-A. Gabriel,
1004 2017, Extreme scale multi-physics simulations of the tsunamigenic 2004 sumatra
1005 megathrust earthquake, *Proc. Int. Conf. High Perform. Comput. Networking, Storage Anal.*
1006 - SC '17, no. November, 1–16, doi: 10.1145/3126908.3126948.
- 1007 Vavryčuk, V., 2015, Moment tensor decompositions revisited, *J. Seismol.*, 19, no. 1, 231–252,
1008 doi: 10.1007/s10950-014-9463-y.

- 1009 Viesca, R. C., and J. R. Rice, 2012, Nucleation of slip-weakening rupture instability in landslides
1010 by localized increase of pore pressure, *J. Geophys. Res. Solid Earth*, 117, no. 3, doi:
1011 10.1029/2011JB008866.
- 1012 Wang, Y., G. Ouillon, J. Woessner, D. Sornette, and S. Husen, 2013, Automatic reconstruction
1013 of fault networks from seismicity catalogs including location uncertainty, *J. Geophys. Res.*
1014 *Solid Earth*, 118, no. 11, 5956–5975, doi: 10.1002/2013JB010164.
- 1015 Wessel, P., W. H. F. Smith, R. Scharroo, J. Luis, and F. Wobbe, 2013, Generic Mapping Tools:
1016 Improved Version Released, *Eos, Trans. Am. Geophys. Union*, 94, no. 45, 409–410, doi:
1017 10.1002/2013EO450001.
- 1018 Wolf, Sebastian, A.-A. Gabriel, and M. Bader, 2020, Optimisation and Local Time Stepping of
1019 an ADER-DG Scheme for Fully Anisotropic Wave Propagation in Complex Geometries, in
1020 *Proceedings of the 10th International Workshop on Advances in High-Performance*
1021 *Computational Earth Sciences: Applications and Frameworks*, preprint available at
1022 <https://wolke.geophysik.uni-muenchen.de/s/ReaBg7mjabPwwLk#pdfviewer>.
- 1023 Wollherr, S., A. Gabriel, and P. M. Mai, 2019, Landers 1992 “Reloaded”: Integrative Dynamic
1024 Earthquake Rupture Modeling, *J. Geophys. Res. Solid Earth*, 124, no. 7, 6666–6702, doi:
1025 10.1029/2018JB016355.
- 1026 Wollherr, S., A. A. Gabriel, and C. Uphoff, 2018, Off-fault plasticity in three-dimensional
1027 dynamic rupture simulations using a modal Discontinuous Galerkin method on unstructured
1028 meshes: Implementation, verification and application, *Geophys. J. Int.*, 214, no. 3, 1556–
1029 1584, doi: 10.1093/GJI/GGY213.

- 1030 Woo, J. -U., M. Kim, D. -H. Sheen, T. -S. Kang, J. Rhie, F. Grigoli, W. L. Ellsworth, and D.
1031 Giardini, 2019, An In-Depth Seismological Analysis Revealing a Causal Link Between the
1032 2017 M_w 5.5 Pohang Earthquake and EGS Project, *J. Geophys. Res. Solid Earth*,
1033 2019JB018368, doi: 10.1029/2019JB018368.
- 1034 Yamashita, T., and Y. Umeda, 1994, Earthquake rupture complexity due to dynamic nucleation
1035 and interaction of subsidiary faults, *Pure Appl. Geophys. PAGEOPH*, 143, nos. 1–3, 89–
1036 116, doi: 10.1007/BF00874325.
- 1037 Zaliapin, I., and Y. Ben-Zion, 2013, Earthquake clusters in southern California I: Identification
1038 and stability, *J. Geophys. Res. Solid Earth*, 118, no. 6, 2847–2864, doi: 10.1002/jgrb.50179.
- 1039 van Zelst, I., S. Wollherr, A. -A. Gabriel, E. H. Madden, and Y. Dinther, 2019, Modeling
1040 Megathrust Earthquakes Across Scales: One-way Coupling From Geodynamics and
1041 Seismic Cycles to Dynamic Rupture, *J. Geophys. Res. Solid Earth*, 124, no. 11, 11414–
1042 11446, doi: 10.1029/2019JB017539.
- 1043 Zhan, Z., 2019, Distributed acoustic sensing turns fiber-optic cables into sensitive seismic
1044 antennas, *Seismol. Res. Lett.*, 91, no. 1, 1–15, doi: 10.1785/0220190112.
- 1045 Zhang, Q., and P. M. Shearer, 2016, A new method to identify earthquake swarms applied to
1046 seismicity near the San Jacinto Fault, California, *Geophys. J. Int.*, 205, no. 2, 995–1005,
1047 doi: 10.1093/gji/ggw073.
- 1048 Ziegler, M. O., O. Heidbach, A. Zang, P. Martínez-Garzón, and M. Bohnhoff, 2017, Estimation
1049 of the differential stress from the stress rotation angle in low permeable rock, *Geophys. Res.*
1050 *Lett.*, 44, no. 13, 6761–6770, doi: 10.1002/2017GL073598.

1051

1052 **FULL AUTHOR'S MAILING LIST:**

1053 Kadek Hendrawan Palgunadi : kadek.palgunadi@kaust.edu.sa

1054 Alice-Agnes Gabriel : gabriel@geophysik.uni-muenchen.de

1055 Thomas Ulrich : ulrich@geophysik.uni-muenchen.de

1056 José Ángel López-Comino : lopezcomino@uni-potsdam.de

1057 Paul Martin Mai : martin.mai@kaust.edu.sa

1058

1059 **LIST OF TABLE CAPTIONS:**

1060 **Table A1.** Fault friction parameters assumed in this study

1061

1062 **LIST OF FIGURE CAPTIONS:**

1063 **Figure 1.** Map of the South Korean Peninsula showing the near-regional broadband stations (blue
1064 triangles). Solid and dashed lines represent the Yangsan and interpreted geological faults near the
1065 Pohang EGS site, respectively. The two inset plots present the location and geometry of the faults
1066 of Model 1F (upper panel) and Model 2F (lower panel). The thicker black lines mark the near-
1067 surface edge of the fault planes. Colored dots depict aftershocks locations extracted from Kim et
1068 al. (2018). The non-double-couple solution of Grigoli et al. (2018) is also shown.

1069

1070 **Figure 2.** Fault reconstruction using guided anisotropic location uncertainty distribution (g-
1071 ACLUD). a) Spatiotemporal density plot of the mainshock and aftershocks based on the nearest-
1072 neighbor distance. b), c) and d) Two fault plane geometry inferred by the g-ACLU method. The
1073 main fault plane has a strike of 214° and dips at 65° , while the secondary fault plane has a strike

1074 199° and dips at 60°. Black dots depict the seismicity used in this study. The geometry of the faults
1075 is shown in views b) as view from North, in c) as view from South, and d) in map view. The red
1076 star denotes the hypocenter of the Pohang earthquake.

1077

1078 **Figure 3.** 3D rendering of the unstructured tetrahedral computational mesh, and the fault plane
1079 with final slip on the 2-fault preferred model (Model 2F) of the Pohang earthquake (warm colors,
1080 in m), and the radiated seismic wavefield 5 seconds after rupture initiation (cold colors, absolute
1081 particle velocity in m/s). Note the strong effect of the high-resolution topography on modulating
1082 the seismic wavefield.

1083

1084 **Figure 4.** Graphical summary of the outcome of 180 dynamic rupture simulations assuming
1085 different combinations of initial relative prestress ratio (R_0), fluid-pressure ratio (γ) and direction
1086 of S_{Hmax} . The corresponding 180 square frames are filled with color if the combination of
1087 parameters is able to trigger self-sustained rupture beyond the nucleation region on any fault. The
1088 S_{Hmax} direction is indicated by the size of the frame, leading to six imbricated frames for each set
1089 of prestress and fluid-pressure ratio parameters.

1090

1091 **Figure 5.** Overview of the simulated earthquake rupture of the preferred model (Model 2F),
1092 showing in a) and b) the space-time evolutions of the absolute slip-rate (in m/s) across the main
1093 and secondary fault plane. a) (left panel) view from North displaying the main fault rupture.
1094 Snapshots every 0.1 s. (right panel) view from South highlighting the rupture of a portion of the
1095 secondary fault. Snapshots every 0.05 s. b-c) Rupture-time contours at intervals of 0.2 s.

1096

1097 **Figure 6.** Moment rate release of a) Model 1F and b) Model 2F and moment tensor
1098 representation of the preferred one-fault c) and two-fault d) models.

1099

1100 **Figure 7.** Distribution of absolute fault slip (in m) in a) and b), and rake angles (in degrees) in c)
1101 and d) for the preferred dynamic rupture scenario (Model 2F) a) and c) view from North
1102 highlighting the main fault rupture. b) and d) view from South highlighting the rupture of a portion
1103 of the secondary fault. The white star in panel a) marks the considered hypocenter location.

1104

1105 **Figure 8.** Comparison of synthetic and observed ground motion waveforms. a) Distribution of
1106 virtual stations (green triangles) at which synthetic waveforms are compared in b). The beachball
1107 is the moment tensor representation of the preferred 2 planes model scenario (Model 2F). Solid
1108 and dashed red lines represent the mapped Yangsan fault surface trace and the interpreted fault
1109 traces near the Pohang EGS site, respectively. The two rectangles show the location and geometry
1110 of the faults used in this study. b) Comparison of synthetic waveforms using one (Model 1F, blue
1111 dashed lines) and two fault planes (Model 2F, red solid lines) at the 19 dummy stations located in
1112 a). A 0.1 - 2 Hz 4th order Butterworth filter is applied to all traces. All traces are normalized. For
1113 each trace, the maximum velocity amplitude (in m/s) of Model 1F is indicated within a black
1114 square. c) Observed (black) and synthetic (red) waveforms for five regional stations for up-down
1115 (UD), east-west (EW) and north-south (NS) components (all located in South Korea, see blue
1116 triangles in Figure 1). $t = 0$ s denotes the origin time of the Pohang earthquake. A 0.033-0.08 Hz
1117 4th order Butterworth filter is applied to all traces. Synthetic regional waveforms are generated
1118 from the preferred dynamic rupture scenario Model 2F using Instaseis (Krischer et al., 2017) and
1119 2 s accurate Green's functions based on the PREM anisotropic model.

1120

1121 **Figure 9.** ((a) and (b)) Co-seismic surface displacements in the InSAR Line-of-sight (LoS)
1122 direction (in m) generated by a) Model 1F; one-plane (rectangle) and b) Model 2F; two-planes
1123 (two rectangles) preferred dynamic rupture scenario, respectively. The dashed red lines represent
1124 the traces of the interpreted faults near the EGS site.

1125

Preprint submitted to EarthArXiv

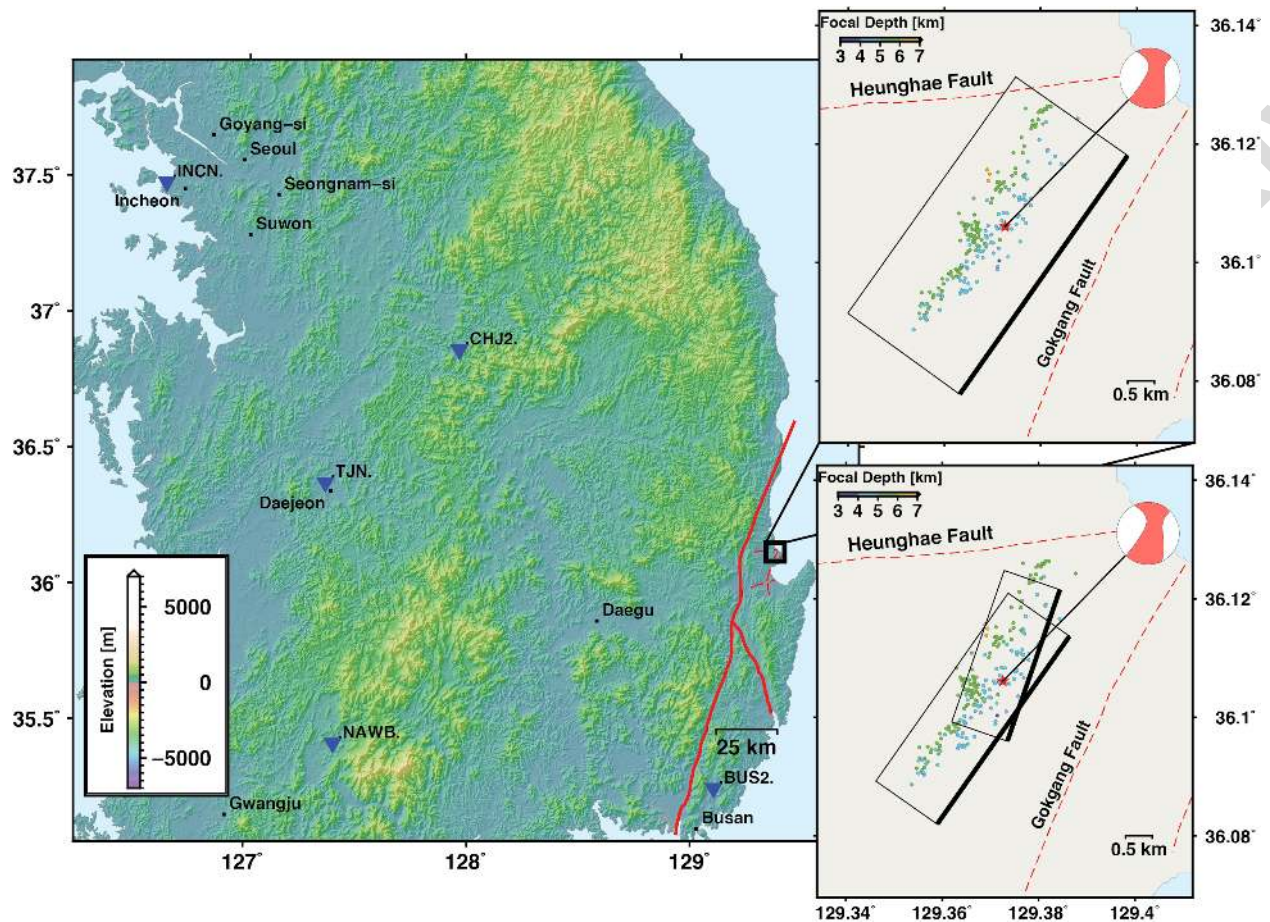
1126 **LIST OF TABLES:**

1127 **Table A1.** Fault friction parameters assumed in this study

Parameter	Symbol	Value
Direct effect parameter	a	0.01 - 0.02 $z \leq 3.3$ km and 0.01 $z > 3.3$ km
Evolution effect parameter	b	0.014
Reference slip velocity	V_0	10^{-6} m/s
Steady-state friction coefficient at V_0	f_0	0.6
State-evolution distance	L	0.2 m
Weakening slip velocity	V_w	0.1 - 1.0 $z \leq 3.3$ km and 0.1 z > 3.3 km
Fully weakened friction coefficient	f_w	0.1
Initial slip rate	V_{ini}	10^{-16} m/s

1128

1129 **LIST OF FIGURES:**

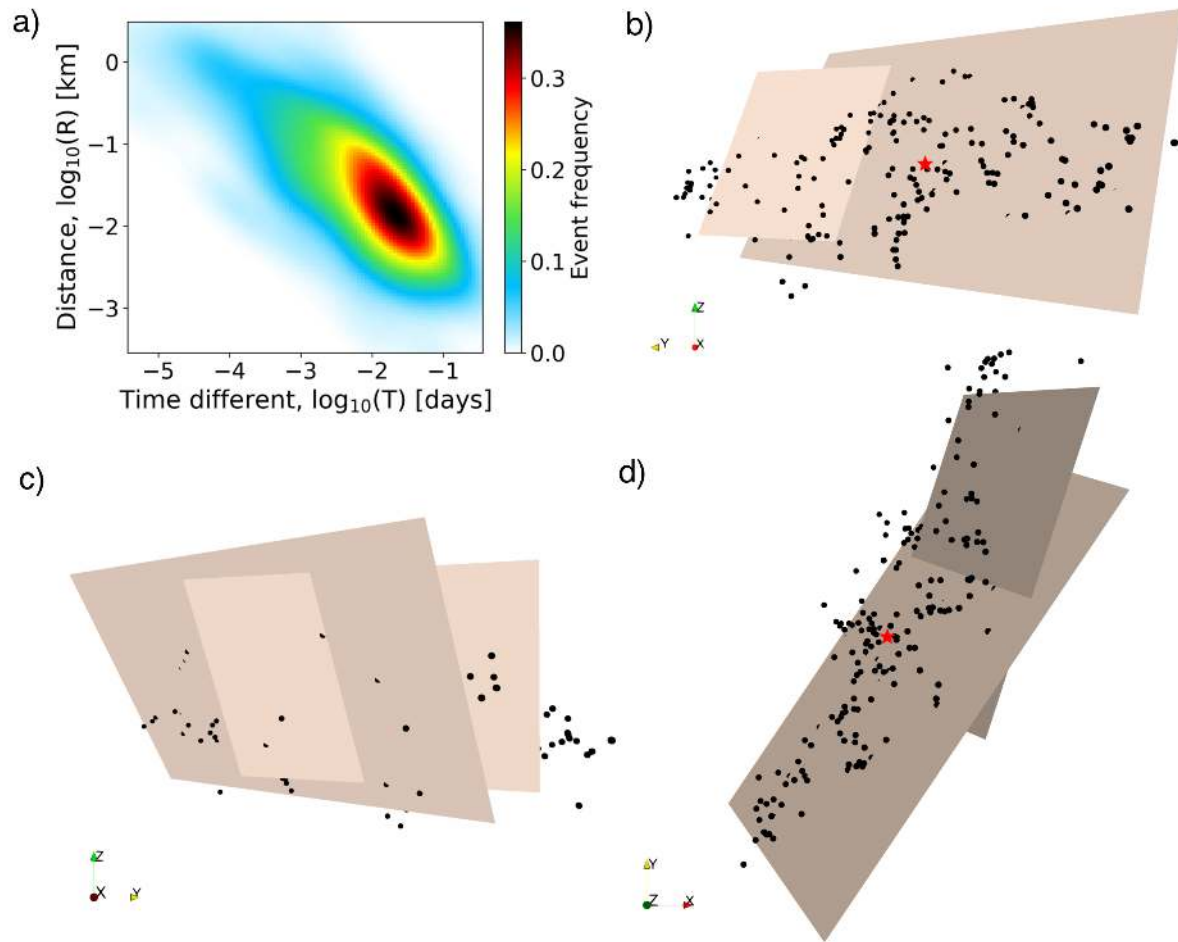


1130

1131 **Figure 1.** Map of the South Korean Peninsula showing the near-regional broadband stations (blue
1132 triangles). Solid and dashed lines represent the Yangsan and interpreted geological faults near the
1133 Pohang EGS site, respectively. The two inset plots present the location and geometry of the faults
1134 of Model 1F (upper panel) and Model 2F (lower panel). The thicker black lines mark the near-
1135 surface edge of the fault planes. Colored dots depict aftershocks locations extracted from Kim et
1136 al. (2018). The non-double-couple solution of Grigoli et al. (2018) is also shown.

1137

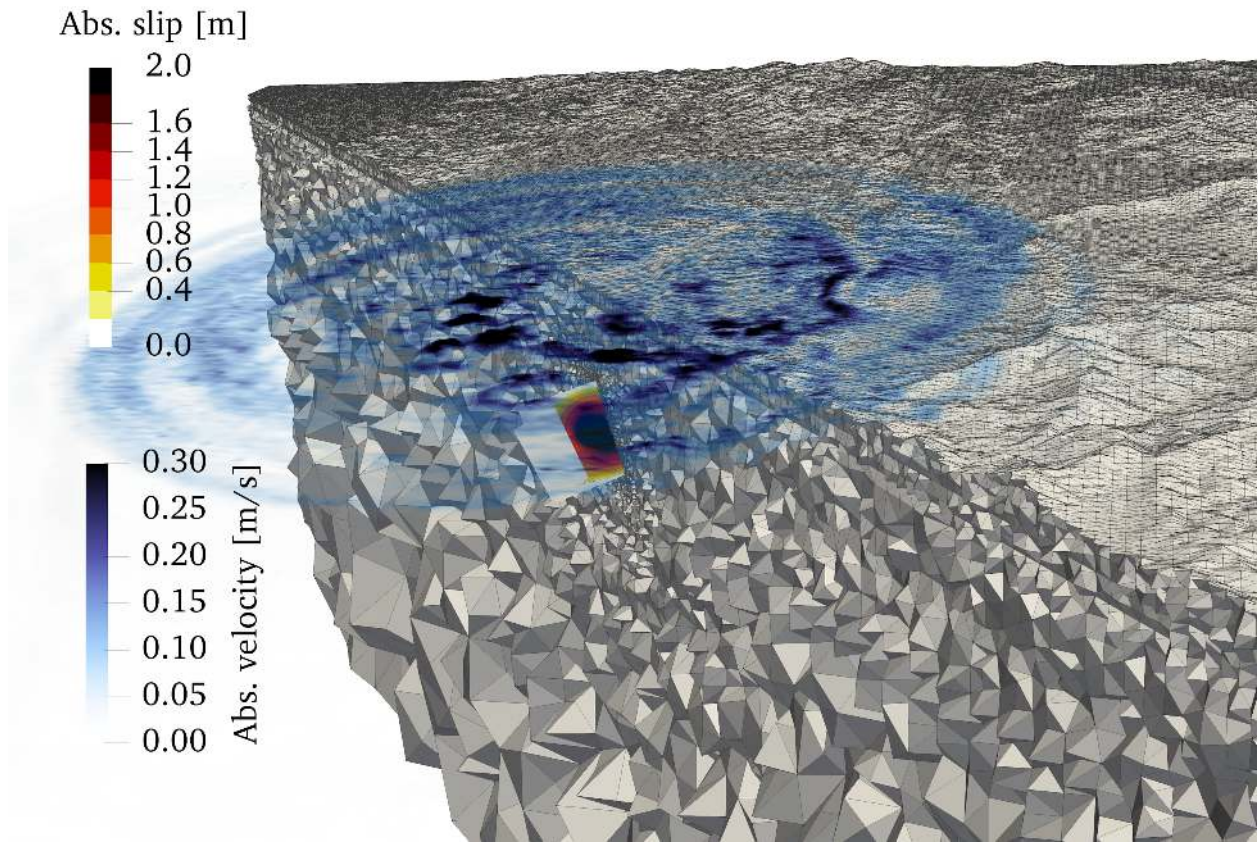
1138



1139

1140 **Figure 2.** Fault reconstruction using guided anisotropic location uncertainty distribution (g-
1141 ACLUD). a) Spatiotemporal density plot of the mainshock and aftershocks based on the nearest-
1142 neighbor distance. b), c) and d) Two fault plane geometry inferred by the g-ACLUD method. The
1143 main fault plane has a strike of 214° and dips at 65°, while the secondary fault plane has a strike
1144 199° and dips at 60°. Black dots depict the seismicity used in this study. The geometry of the faults
1145 is shown in views b) as view from North, in c) as view from South, and d) in map view. The red
1146 star denotes the hypocenter of the Pohang earthquake.

1147

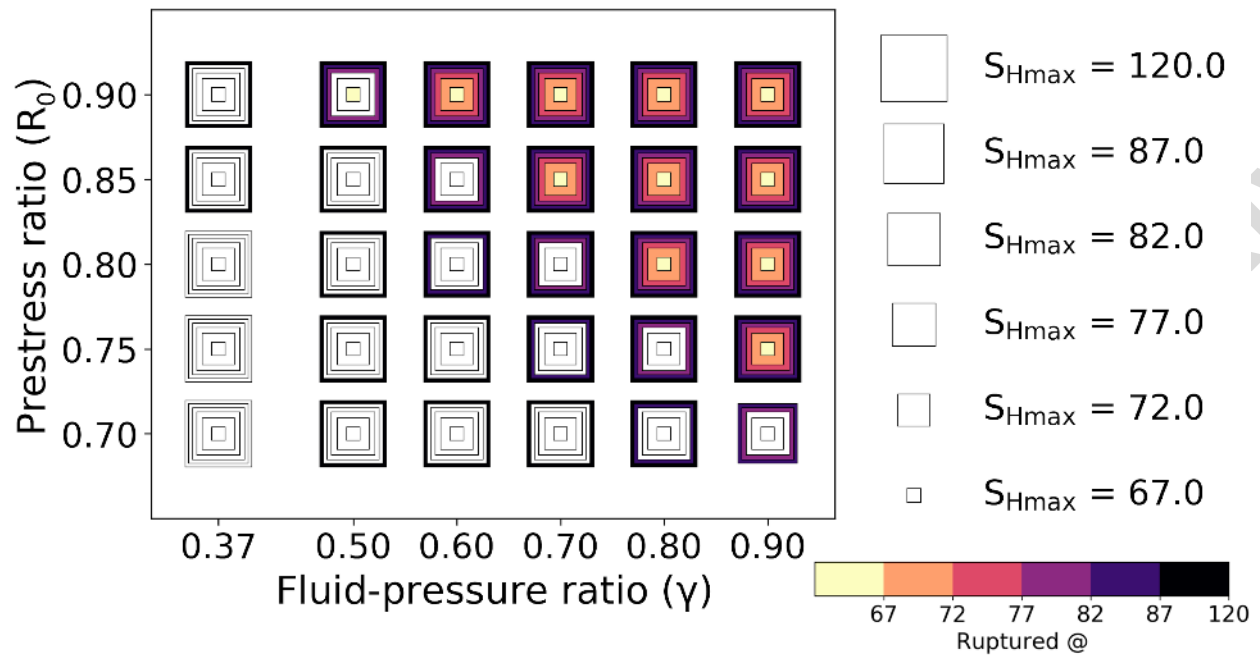


1148

1149 **Figure 3.** 3D rendering of the unstructured tetrahedral computational mesh, and the fault plane
1150 with final slip on the 2-fault preferred model (Model 2F) of the Pohang earthquake (warm colors,
1151 in m), and the radiated seismic wavefield 5 seconds after rupture initiation (cold colors, absolute
1152 particle velocity in m/s). Note the strong effect of the high-resolution topography on modulating
1153 the seismic wavefield.

1154

1155

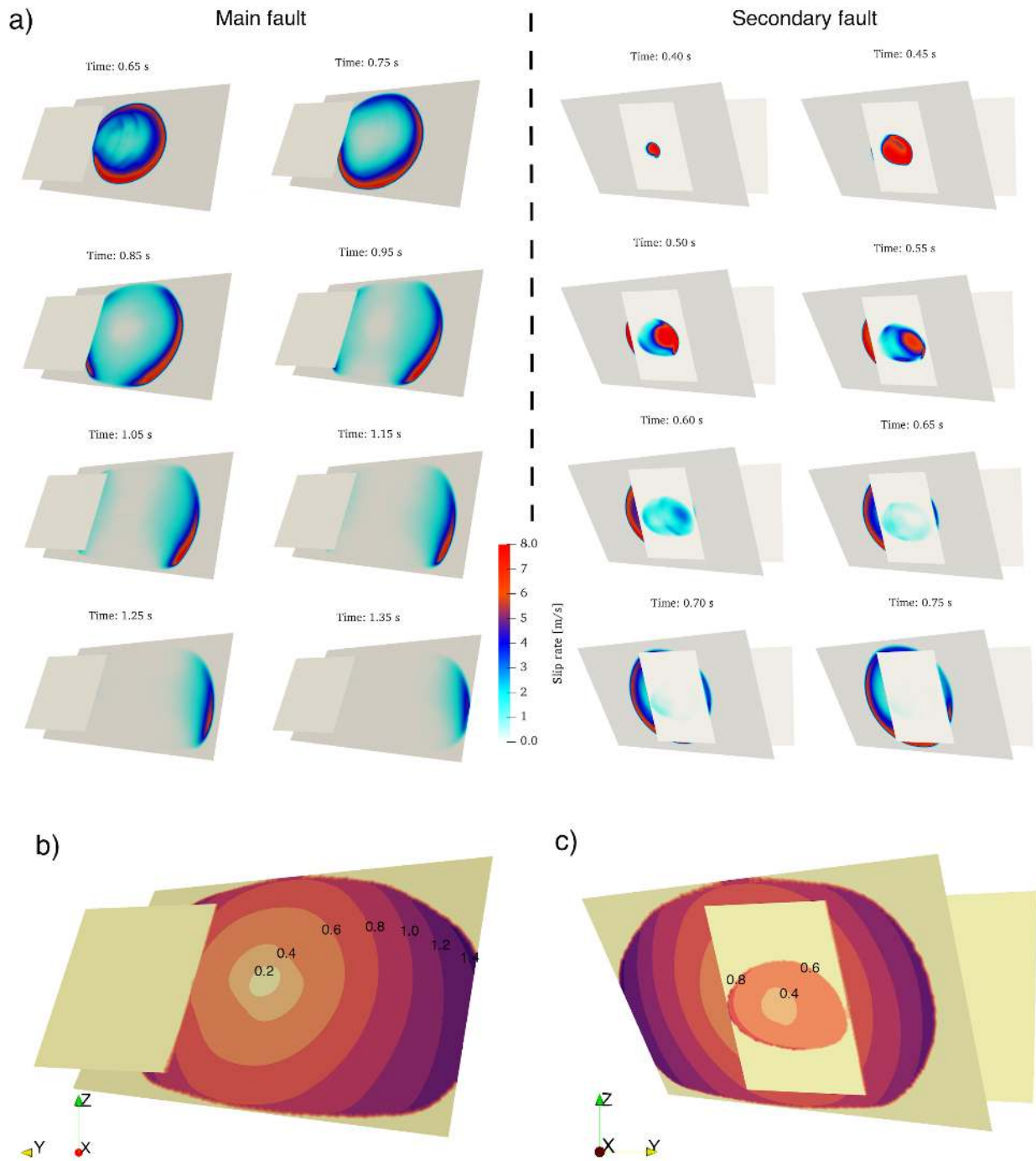


1156

1157 **Figure 4.** Graphical summary of the outcome of 180 dynamic rupture simulations assuming
 1158 different combinations of initial relative prestress ratio (R_0), fluid-pressure ratio (γ) and direction
 1159 of S_{Hmax} . The corresponding 180 square frames are filled with color if the combination of
 1160 parameters is able to trigger self-sustained rupture beyond the nucleation region on any fault. The
 1161 S_{Hmax} direction is indicated by the size of the frame, leading to six imbricated frames for each set
 1162 of prestress and fluid-pressure ratio parameters.

1163

1164



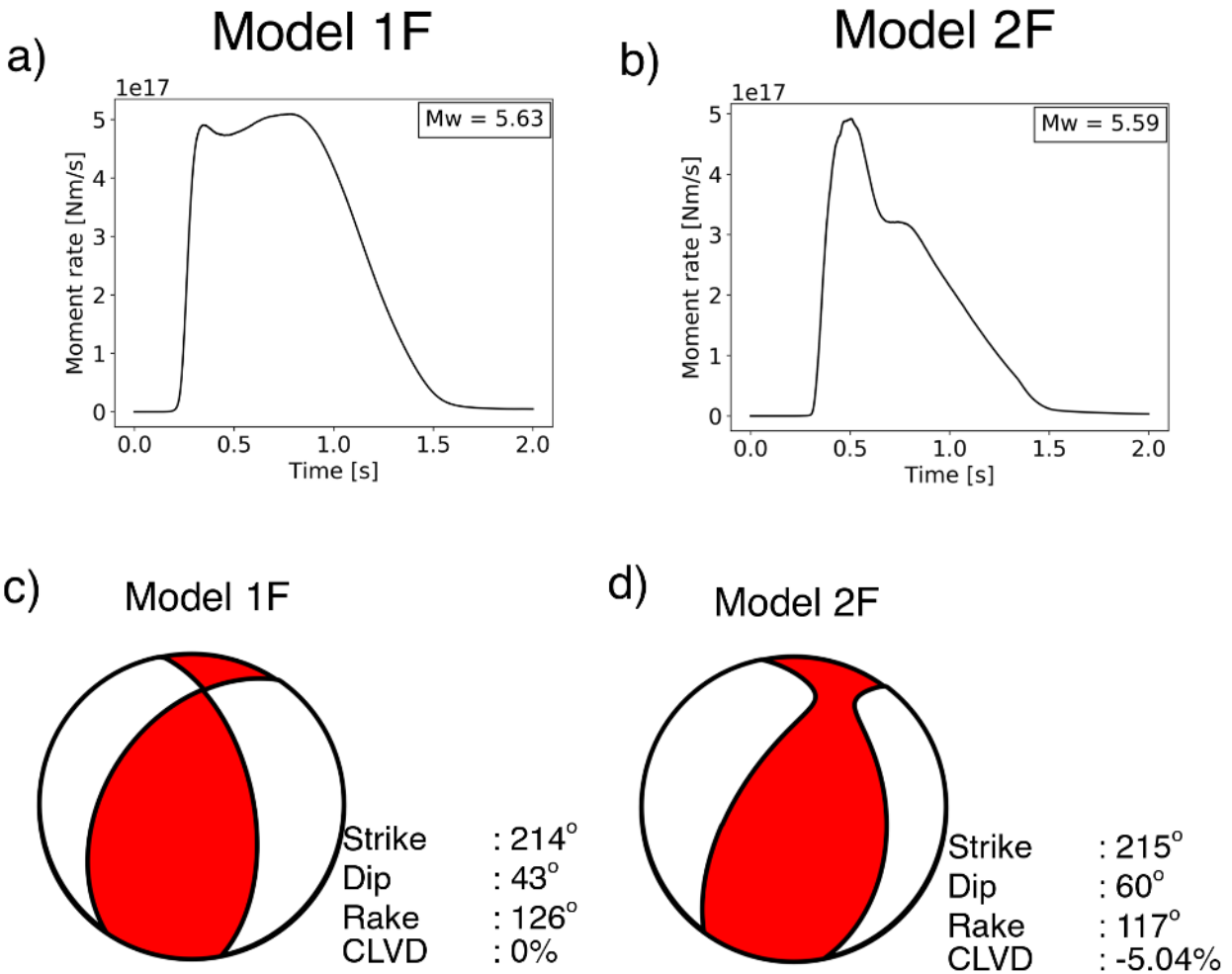
1165

1166

1167 **Figure 5.** Overview of the simulated earthquake rupture of the preferred model (Model 2F),

1168 showing in a) and b) the space-time evolutions of the absolute slip-rate (in m/s) across the main

1169 and secondary fault plane. a) (left panel) view from North displaying the main fault rupture.
 1170 Snapshots every 0.1 s. (right panel) view from South highlighting the rupture of a portion of the
 1171 secondary fault. Snapshots every 0.05 s. b-c) Rupture-time contours at intervals of 0.2 s.
 1172

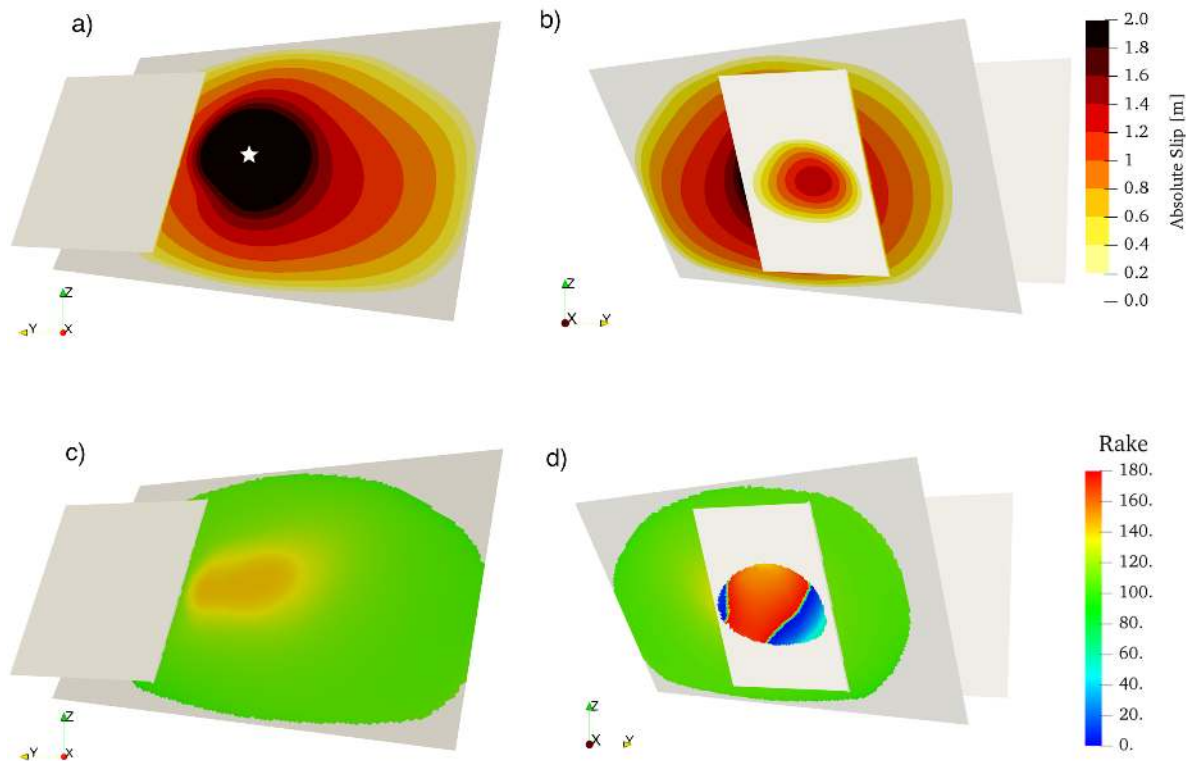


1173

1174 **Figure 6.** Moment rate release of a) Model 1F and b) Model 2F and moment tensor

1175 representation of the preferred one-fault c) and two-fault d) models.

1176



1177

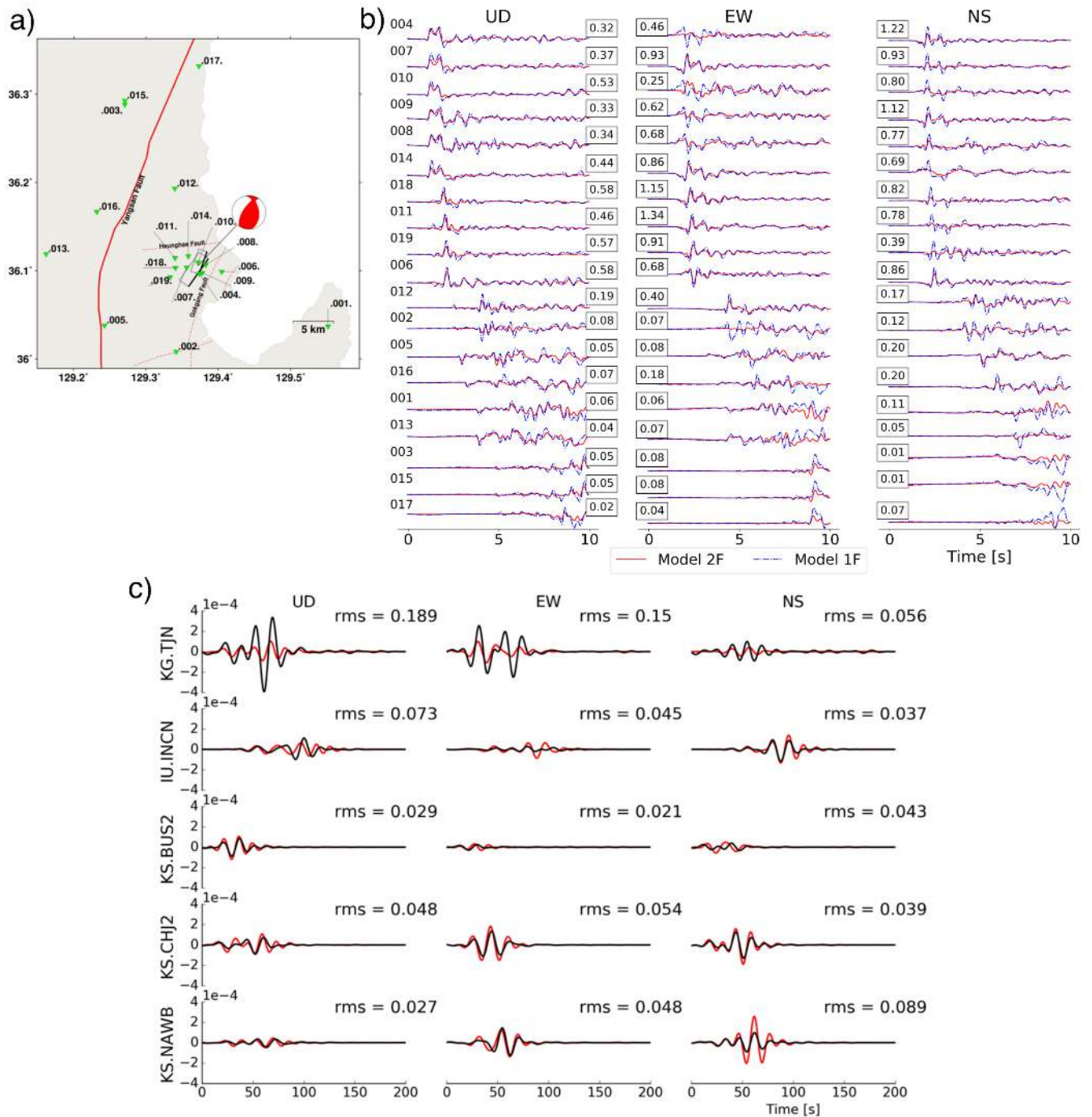
1178 **Figure 7.** Distribution of absolute fault slip (in m) in a) and b), and rake angles (in degrees) in c)
1179 and d) for the preferred dynamic rupture scenario (Model 2F) a) and c) view from North
1180 highlighting the main fault rupture. b) and d) view from South highlighting the rupture of a portion
1181 of the secondary fault. The white star in panel a) marks the considered hypocenter location.

1182

1183

1184

1185



1186

1187 **Figure 8.** Comparison of synthetic and observed ground motion waveforms. a) Distribution of
 1188 virtual stations (green triangles) at which synthetic waveforms are compared in b). The beachball
 1189 is the moment tensor representation of the preferred 2 planes model scenario (Model 2F). Solid
 1190 and dashed red lines represent the mapped Yangsan fault surface trace and the interpreted fault

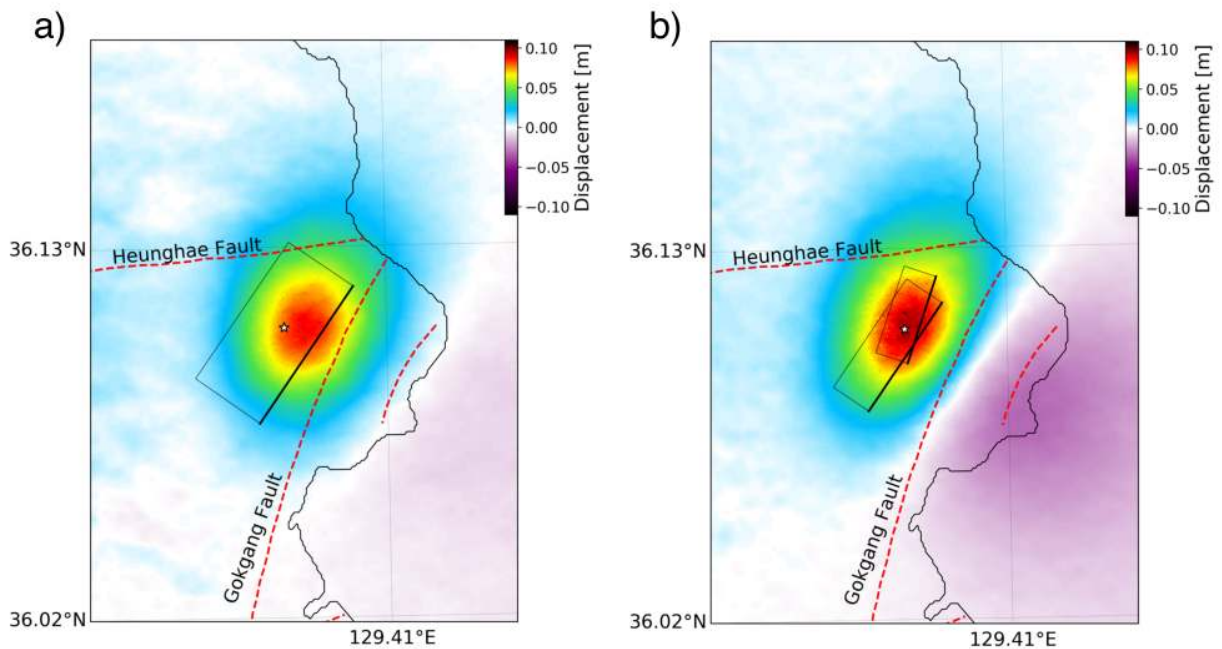
1191 traces near the Pohang EGS site, respectively. The two rectangles show the location and geometry
1192 of the faults used in this study. b) Comparison of synthetic waveforms using one (Model 1F, blue
1193 dashed lines) and two fault planes (Model 2F, red solid lines) at the 19 dummy stations located in
1194 a). A 0.1 - 2 Hz 4th order Butterworth filter is applied to all traces. All traces are normalized. For
1195 each trace, the maximum velocity amplitude (in m/s) of Model 1F is indicated within a black
1196 square. c) Observed (black) and synthetic (red) waveforms for five regional stations for up-down
1197 (UD), east-west (EW) and north-south (NS) components (all located in South Korea, see blue
1198 triangles in Figure 1). $t = 0$ s denotes the origin time of the Pohang earthquake. A 0.033-0.08 Hz
1199 4th order Butterworth filter is applied to all traces. Synthetic regional waveforms are generated
1200 from the preferred dynamic rupture scenario Model 2F using Instaseis (Krischer et al., 2017) and
1201 2 s accurate Green's functions based on the PREM anisotropic model.

1202

1203

1204

1205



1206

1207 **Figure 9.** ((a) and (b)) Co-seismic surface displacements in the InSAR Line-of-sight (LoS)
1208 direction (in m) generated by a) Model 1F; one-plane (rectangle) and b) Model 2F; two-planes
1209 (two rectangles) preferred dynamic rupture scenario, respectively. The dashed red lines represent
1210 the traces of the interpreted faults near the EGS site.

1211

1212 APPENDIX

1213 Friction parameters

1214 To parameterize the frictional behavior, we use laboratory-based rapid velocity weakening friction
1215 law proposed by the community benchmark problem TPV104 Southern California Earthquake
1216 Center (SCEC-benchmark) (Harris et al., 2018). The friction law is adapted from - the formulation
1217 introduced by Dunham et al. (2011a). The governing equations in our notation are described in
1218 Ulrich et al. (2019a), the implementation in SeisSol (see **Data and Resources**) is described and
1219 verified in Pelties et al. (2014). Figure S1b shows the depth-dependent direct effect a and

1220 weakening slip velocity V_W . The evolution effect parameter b is set constant. We apply a velocity
 1221 strengthening zone at the top 200 m of all faults to smoothly stop rupture. Within this zone, values
 1222 for a and V_W increase linearly ranging from 0.01 and 0.1 m/s below depth of 3.3 km to 0.02 and
 1223 1.0 m/s to the surface, respectively. Table A1 lists all friction parameters used in this study.

1224

1225 **Table A1.** Fault friction parameters assumed in this study

Parameter	Symbol	Value
Direct effect parameter	a	0.01 - 0.02 $z \leq 3.3$ km and 0.01 $z > 3.3$ km
Evolution effect parameter	b	0.014
Reference slip velocity	V_0	10^{-6} m/s
Steady-state friction coefficient at V_0	f_0	0.6
State-evolution distance	L	0.2 m
Weakening slip velocity	V_W	0.1 - 1.0 $z \leq 3.3$ km and 0.1 z > 3.3 km
Fully weakened friction coefficient	f_W	0.1
Initial slip rate	V_{ini}	10^{-16} m/s

1226

1227

1228

1229 **Nucleation procedure**

1230 To nucleate the earthquake, we apply a time-dependent overstress centered at the hypocenter
1231 location, that is at longitude and latitude of 129.37° and 36.11° , respectively, and at a depth of 4.27
1232 km. The time-dependent overstressed nucleation area $R_{nuc}(t)$ is determined by increasing the
1233 initial relative prestress ratio R_0 as:

1234

1235
$$R_{nuc}(t) = R_0 + \Omega(r) \times S(t) \quad (A1)$$

1236

1237 where $\Omega(r)$ is a Gaussian-step function, r is the radius from the hypocenter, and $S(t)$ denotes the
1238 smoothed step function. The Gaussian-step function is defined as:

1239

1240
$$\Omega(r) = \xi \exp\left(\frac{r^2}{r^2 - r_c^2}\right) \quad \text{for } r < r_c; \quad \Omega(r) = 0 \quad \text{otherwise} \quad (A2)$$

1241

1242 where ξ is the overstressed initial relative prestress ratio and $r_c = 500\text{m}$ is the radius of the
1243 nucleation patch. We only overstress the main fault plane; In the nucleation region, we set ξ to 2,
1244 and apply an overstress characterized by $S_{Hmax} = 77^\circ$ and $\nu = 0.1$. These values are set by trial-
1245 and-error to allow rupture to propagate spontaneously with the least magnitude of overstress and
1246 to limit fault slip inside the nucleation patch. The orientation of S_{Hmax} is also in accordance with
1247 Korean Government Commission, 2019 and Ellsworth et al. (2019) which suggest optimally
1248 oriented stress orientation and critically stressed inside the nucleation zone. The smoothed step
1249 function is formulated as:

1250

1251
$$S(t) = \exp\left(\frac{(t-T)^2}{t \times (t-2 \times T)}\right) \quad \text{for } 0 < t < T; S(t) = 1 \quad \text{for } t \geq T \quad (\text{A3})$$

1252

1253 where $T = 0.4$ s is the nucleation time.

1254

1255 **Numerical method**

1256 We use the open-source software SeisSol (Dumbser and Käser, 2006; Pelties et al., 2014; Uphoff
1257 et al., 2017; Wollherr et al., 2018) (see **Data and Resources**), which couples seismic wave
1258 propagation in complex media and frictional fault failure. SeisSol uses an Arbitrary high-order
1259 DERivative-Discontinuous Galerkin (ADER-DG) approach which achieves high-order accuracy
1260 in space and time (Käser and Dumbser, 2006). SeisSol uses flexible non-uniform unstructured
1261 tetrahedral mesh, which allows accounting for complex geometric features such as 3D fault
1262 networks or high-resolution topography across a large range of scales: from small-scale fault
1263 roughness, large-scale fault structures to fault-to-fault interaction. Dynamic rupture simulations
1264 are sensitive to geometric complexity of faults (Dunham et al., 2011b; Shi and Day, 2013;
1265 Uphoff et al., 2017; Wollherr et al., 2018, 2019; Ulrich et al., 2019a, 2019b).

1266 A high resolution and accurate simulation are essential to resolve the detailed processes of
1267 rupture propagation of the intersected fault geometry. We motivate the presented deterministic
1268 parameter study with the computational feasibility of many such simulations. While the feasibility
1269 of dynamic rupture inversion and statistical learning approaches has been demonstrated (e.g.
1270 Peyrat et al. 2001; Bauer et al., 2018, Happ et al. 2019, Gallovič et al. 2019a, Gallovič et al. 2019b),

1271 these are restricted by near-field data availability and the computational cost of each forward
1272 dynamic rupture model.

1273 SeisSol is verified in a wide range of benchmark problems, including dipping faults,
1274 branched and curved faults, on-fault heterogeneity, and laboratory-based friction laws (de la
1275 Puente et al., 2009; Pelties et al., 2012; Pelties et al., 2014; Wollherr et al., 2018,) in line with the
1276 SCEC-Benchmark Dynamic Rupture code verification exercises (Harris et al., 2011; Harris et al.,
1277 2018) as well as against analytical reference solutions for seismic wave propagation (e.g., Uphoff
1278 and Bader, 2016; Wolf et al., 2020). Fast time to solution is achieved using end-to-end optimization
1279 (Breuer et al., 2014; Heinecke et al., 2014; Rettenberger et al., 2016), including an efficient local
1280 time-stepping algorithm (Breuer et al., 2016, Uphoff et al., 2017). This efficient algorithm on high-
1281 performance computing architecture provides up to ten-fold speed up (Uphoff et al., 2017).

1282 SeisSol allows accounting for off-fault yielding. Inelastic energy dissipation influences
1283 rupture dynamics such as rupture speed and rupture style (e.g., Gabriel et al., 2013). Off-fault
1284 plasticity is incorporated using the off-line code generator to compute matrix operations in an
1285 efficient way (Wollherr et al., 2018). SeisSol also supports visco-elastic rheologies, using an off-
1286 line code generator similar to that off-fault plasticity. In this study, we use a spatiotemporal
1287 discretization of polynomial degree $p = 4$ ($O5$) for all simulations.

1288

1289 **Mesh generation**

1290 The simulation domain and fault plane geometry model are created using third-party software
1291 GoCad (Emerson paradigm holding, 2018) in a Cartesian coordinate system. We discretize the
1292 unstructured tetrahedral mesh using the meshing software Simmodeler (Simmetrix Inc., 2017).
1293 The mesh element edge length size to 50 m close to the fault plane and 200 m at the surface

1294 topography, yielding a 4 million volume cell mesh. The mesh size on the fault plane is examined
1295 prior to the simulation by calculating the cohesive zone (or process zone) to ensure convergence.
1296 Wollherr et al. (2018, 2019) provide a way to resolve the cohesive zone for the case of SeisSol. To
1297 save the computational costs and at the same time avoid reflection from the domain boundary, we
1298 gradually increase the edge length size of the tetrahedral element by a factor of 6% away from the
1299 fault plane and surface topography. Figure 3 depicts the unstructured tetrahedral mesh used in this
1300 study, overlain by a snapshot of the absolute velocity field at simulation time 5 s, for our preferred
1301 dynamic rupture model (Model 2F), highlighting the effect of the topography on the near-field
1302 ground motions.

1303 The locally refined mesh and high-order spatiotemporal discretization allow capturing the
1304 high-frequency content of the waveforms with high accuracy (little numerical dispersion),
1305 especially in the near-fault region. We estimate the maximum resolved frequency is up to 4 Hz
1306 within 7 km distance from the fault zone, and around 1 Hz at 30 km distance from the fault.
1307 Simulating 5 s typically requires 15 minutes (average run-time) on Intel Haswell cores with 128
1308 nodes using supercomputer Cray XC40 Shaheen-II, King Abdullah University of Science and
1309 Technology, Saudi Arabia.

1310

1311 **Supplemental Material for**

1312 **Dynamic fault interaction during a fluid-injection induced**

1313 **earthquake: The 2017 Mw 5.5 Pohang event**

1314 **K. H. Palgunadi, A.-A Gabriel, T. Ulrich, J. A. Lopéz-Comino, P. M. Mai**

1315

1316 This supplement includes additional figures, a table, a zipped file and videos supporting
1317 the outcome of the study. The figures consist of depth-dependent 1D subsurface material and
1318 friction parameters, part of static modeling, peak slip-rate distribution, off-fault plastic
1319 deformation, synthetic surface displacements, and shake-map. The table contains the rake of initial
1320 traction of two-fault planes geometry using static modeling. The zipped file consists of all
1321 parameters used for the preferred two-fault planes scenario. The videos show snapshots of the slip-
1322 rate in two perspective views (presenting the main and secondary fault plane) of the preferred two-
1323 fault planes scenario.

1324

1325 **LIST OF SUPPLEMENTAL TABLE CAPTIONS:**

1326 **Table S1.** Rake of initial shear traction on the faults of Model 2F

1327

1328 **LIST OF SUPPLEMENTAL FIGURE CAPTIONS:**

1329 **Figure S1.** Vertical profiles of a) the 1-D model of seismic wave speeds by Woo et al. (2019) and
1330 by Korean Government Commission (2019). Panel b) displays the depth-dependent parameters of
1331 the velocity weakening rate-and-state friction law.

1332

1333 **Figure S2.** Rake of initial (at $t=0$) shear traction for exemplary orientations of maximum horizontal
1334 stress S_{Hmax} (see also Table S1). Thrust-faulting is favoured for $S_{Hmax}=120^\circ$. Note that
1335 $S_{Hmax}=77^\circ$ corresponds to the findings of Ellsworth et al. (2019).

1336

1337 **Figure S3.** Peak slip-rate of the Model 2F. The maximum peak slip rate (saturated yellow color)
1338 outside the nucleation zone is 15 m/s. View from a) North and b) South.

1339

1340 **Figure S4.** Asymmetric off-fault plastic deformation for Model 1F (a and b) and for Model 2F (c
1341 and d). a) and c) view from North b) and d) view from South. The accumulated volumetric plastic
1342 strain is mapped into the scalar quantity η as noted by the purple colorbar.

1343

1344 **Figure S5.** Surface displacements. a) Co-seismic surface displacements using only the main fault
1345 plane of Model 2F. Rectangle illustrates the fault plane. b) Residual of Model 2F with respect to
1346 Model 2F by using only the main fault plane. The dashed red lines represent the traces of the
1347 interpreted faults near the EGS site. The white star represents the epicenter of the Pohang
1348 earthquake.

1349

1350 **Figure S6.** Peak ground velocity shake-map (in m/s, based on GMRotD50 (Boore et al., 2006))
1351 for preferred scenario Model 2F, color-contoured 0.2 increments. The white star denotes the
1352 epicenter of the Pohang earthquake.

1353

1354

1355

1356 **LIST OF SUPPLEMENTAL FILES:**

1357 **Video S1.** Slip-rate of Model 2F. The video also can be accessed in

1358 https://drive.google.com/open?id=1nm3HZ_YOD-j8t_YatTFfs9prVKplEExj

1359 **Parameters.zip** (this file contains all parameters used for the preferred Model 2F)

1360

Preprint submitted to EarthArXiv

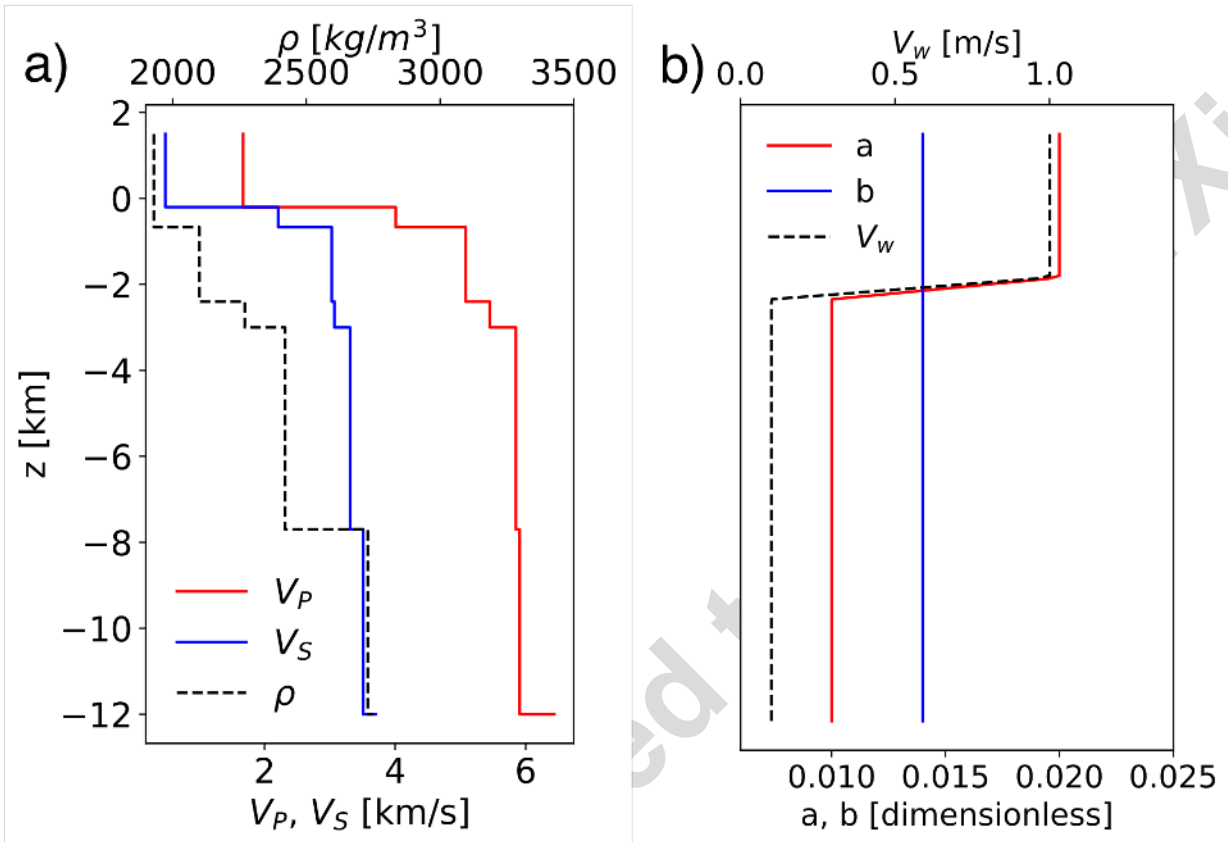
1361 **LIST OF SUPPLEMENTAL TABLES:**

1362 **Table S1.** Rake of initial shear traction on the faults of Model 2F

S_{Hmax}	Main fault rake (°)	Secondary fault rake (°)
52	0	12
57	3	16
62	7	20
67	11	24
72	15	29
77	19	35
82	23	41
87	28	48
92	34	57
97	40	66
102	47	77
107	55	88
112	64	100
120	80	110
125	91	130
130	110	140
135	115	130
140	120	150

1363

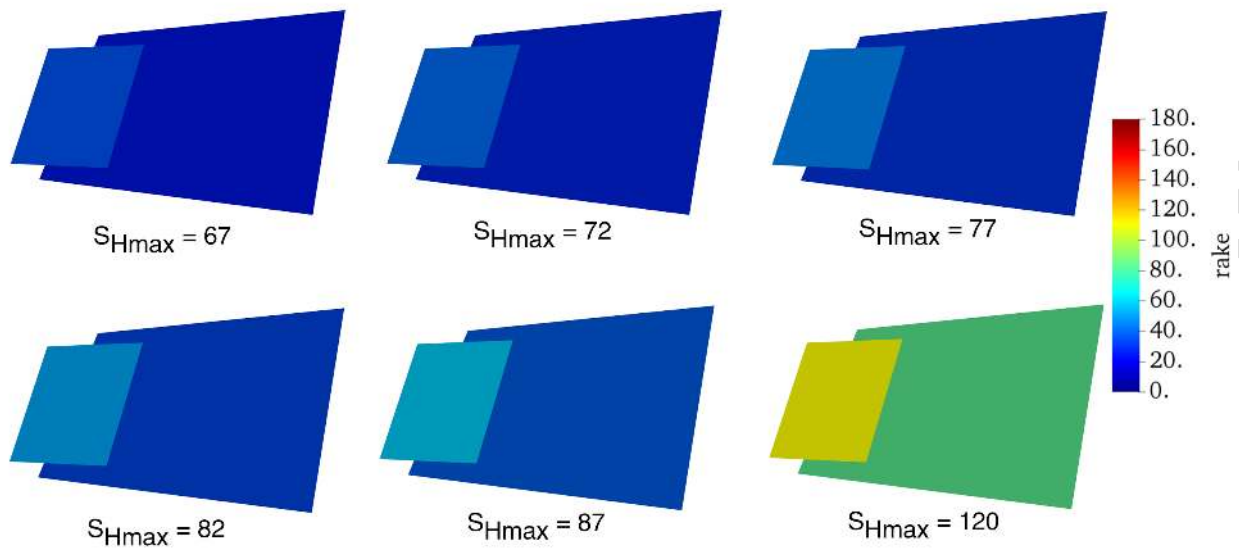
1364 **LIST OF SUPPLEMENTAL FIGURES:**



1365

1366 **Figure S1.** Vertical profiles of a) the 1-D model of seismic wave speeds by Woo et al. (2019) and
1367 by Korean Government Commission (2019). Panel b) displays the depth-dependent parameters of
1368 the velocity weakening rate-and-state friction law.

1369

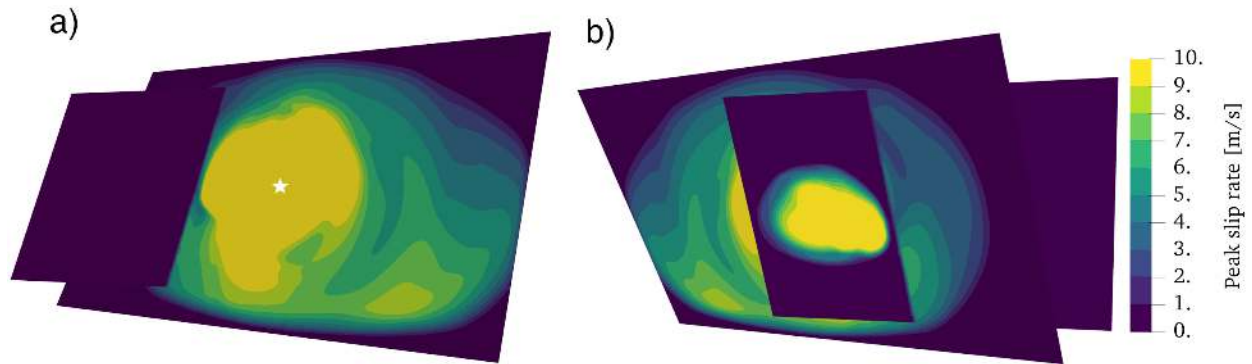


1370

1371 **Figure S2.** Rake of initial (at $t=0$) shear traction for exemplary orientations of maximum horizontal
1372 stress S_{Hmax} (see also Table S1). Thrust-faulting is favoured for $S_{Hmax}=120^\circ$. Note that
1373 $S_{Hmax}=77^\circ$ corresponds to the findings of Ellsworth et al. (2019).

1374

1375



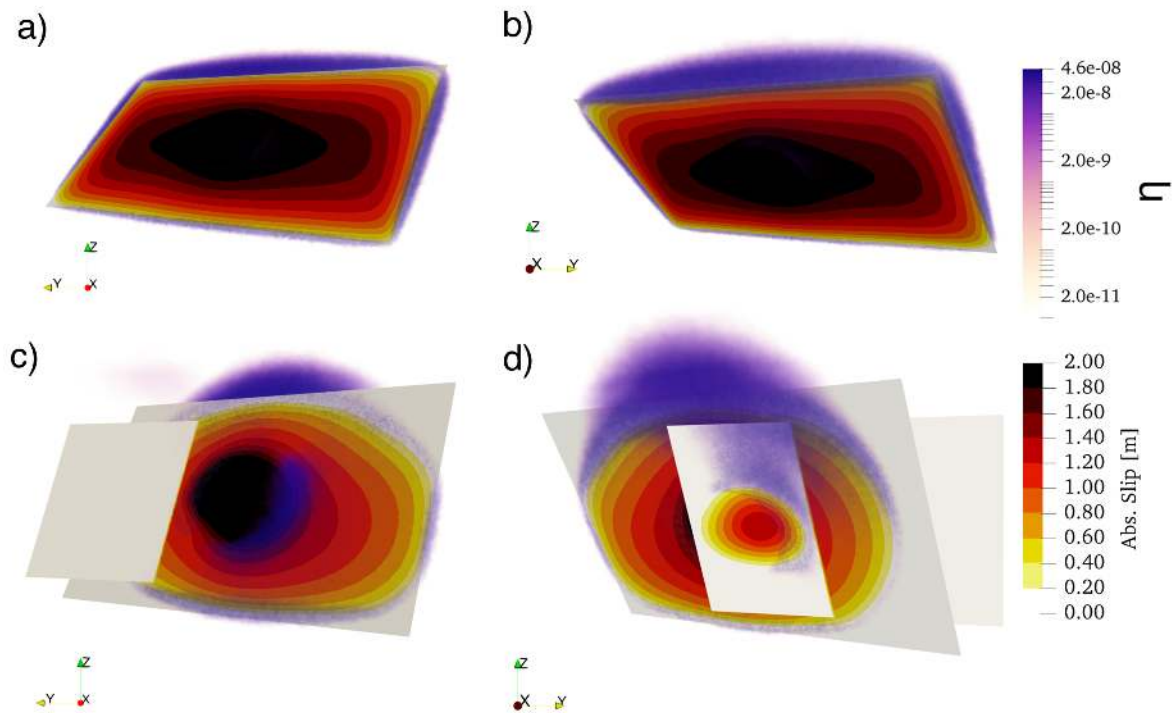
1376

1377 **Figure S3.** Peak slip-rate of the Model 2F. The maximum peak slip rate (saturated yellow color)

1378 outside the nucleation zone is 15 m/s. View from a) North and b) South.

1379

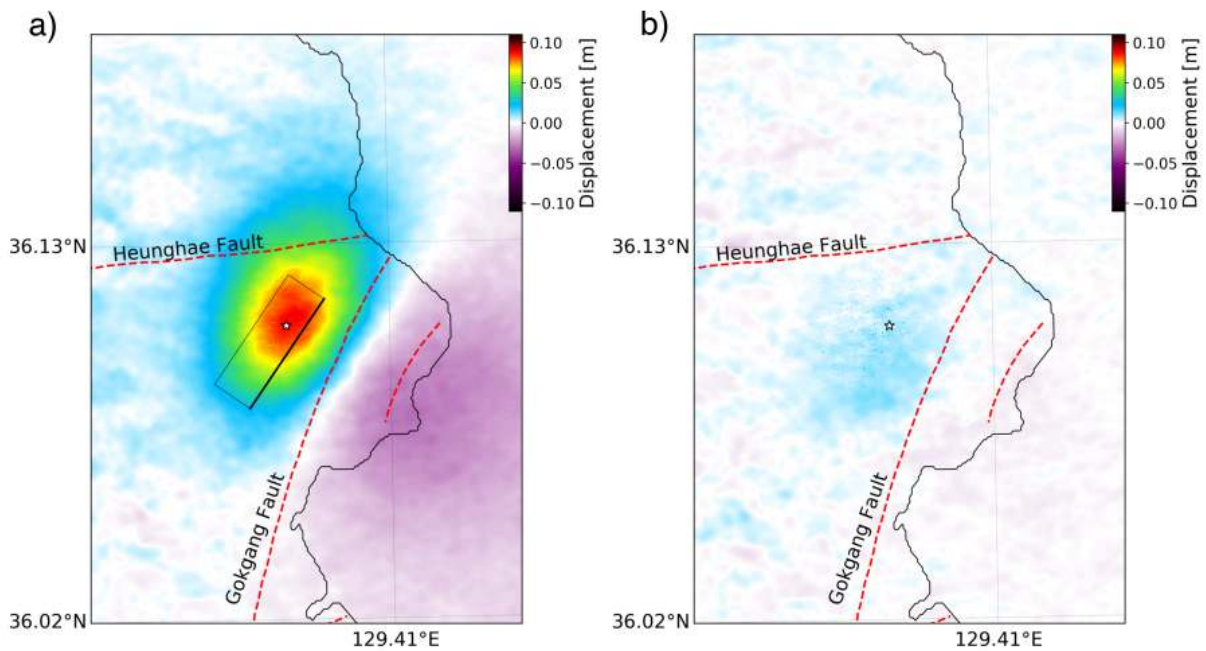
Preprint submitted to Earth



1380

1381 **Figure S4.** Asymmetric off-fault plastic deformation for Model 1F (a and b) and for Model 2F (c
1382 and d). a) and c) view from North b) and d) view from South. The accumulated volumetric plastic
1383 strain is mapped into the scalar quantity η as noted by the purple colorbar.

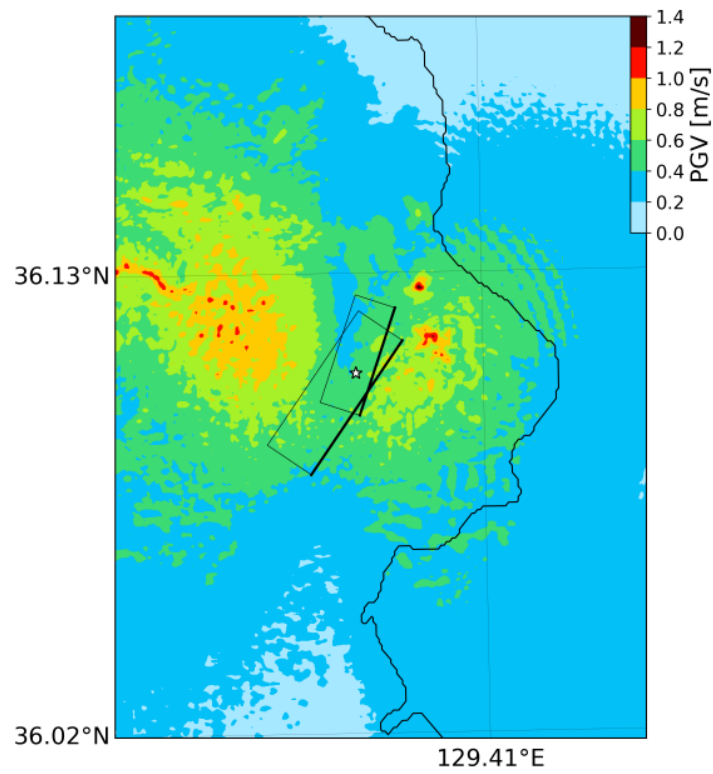
1384



1385

1386 **Figure S5.** Surface displacements. a) Co-seismic surface displacements using only the main fault
1387 plane of Model 2F. Rectangle illustrates the fault plane. b) Residual of Model 2F with respect to
1388 Model 2F by using only the main fault plane. The dashed red lines represent the traces of the
1389 interpreted faults near the EGS site. The white star represents the epicenter of the Pohang
1390 earthquake.

1391



1392

1393 **Figure S6.** Peak ground velocity shake-map (in m/s, based on GMRotD50 (Boore et al., 2006))
1394 for preferred scenario Model 2F, color-contoured 0.2 increments. The white star denotes the
1395 epicenter of the Pohang earthquake.

1396

1397

1398

1399

1400

1401 **References:**

- 1402 Boore, D. M., J. Watson-Lamprey, and N. A. Abrahamson, 2006, Orientation-Independent
1403 Measures of Ground Motion, *Bull. Seismol. Soc. Am.*, 96, no. 4A, 1502–1511, doi:
1404 10.1785/0120050209.
- 1405 Ellsworth, W. L., D. Giardini, J. Townend, S. Ge, and T. Shimamoto, 2019, Triggering of the
1406 Pohang, Korea, Earthquake (Mw 5.5) by enhanced geothermal system stimulation,
1407 *Seismological Society of America*, 1844–1858.
- 1408 Korean Government Commission, 2019, Summary Report of the Korean Government
1409 Commission on Relations between the 2017 Pohang Earthquake and EGS Project.
- 1410 Woo, J. -U., M. Kim, D. -H. Sheen, T. -S. Kang, J. Rhie, F. Grigoli, W. L. Ellsworth, and D.
1411 Giardini, 2019, An In-Depth Seismological Analysis Revealing a Causal Link Between the
1412 2017 M_w 5.5 Pohang Earthquake and EGS Project, *J. Geophys. Res. Solid Earth*,
1413 2019JB018368, doi: 10.1029/2019JB018368.

1414

1415

1416

1417